

1 **Close relatives of MERS-CoV in bats use ACE2 as their functional receptors**

2 Qing Xiong^{1, 5}, Lei Cao^{2, 5}, Chengbao Ma^{1, 5}, Chen Liu¹, Junyu Si¹, Peng Liu¹, Mengxue Gu¹, Chunli Wang¹,
3 Lulu Shi¹, Fei Tong¹, Meiling Huang¹, Jing Li¹, Chufeng Zhao¹, Chao Shen¹, Yu Chen¹, Huabin Zhao⁴, Ke
4 Lan¹, Xiangxi Wang^{2, 3, *}, Huan Yan^{1, *}

5 ¹State Key Laboratory of Virology, Institute for Vaccine Research and Modern Virology Research Center,

6 College of Life Sciences, Wuhan University, Wuhan, Hubei, 430072, China.

7 ² CAS Key Laboratory of Infection and Immunity, National Laboratory of Macromolecules, Institute of
8 Biophysics, Chinese Academy of Sciences, Beijing, 100101, China.

9 ³ University of Chinese Academy of Sciences, Beijing, 100049, China.

10 ⁴ Department of Ecology, Tibetan Centre for Ecology and Conservation at WHU-TU, Hubei Key Laboratory
11 of Cell Homeostasis, College of Life Sciences, Wuhan University, Wuhan 430072, China

12 ⁵ These authors contributed equally to this work.

13 *Correspondence: huanyan@whu.edu.cn, xiangxi@ibp.ac.cn

14

15 **Summary**

16 Middle East Respiratory Syndrome coronavirus (MERS-CoV) and several bat coronaviruses employ
17 Dipeptidyl peptidase-4 (DPP4) as their functional receptors¹⁻⁴. However, the receptor for NeoCoV,
18 the closest MERS-CoV relative yet discovered in bats, remains enigmatic⁵. In this study, we
19 unexpectedly found that NeoCoV and its close relative, PDF-2180-CoV, can efficiently use some
20 types of bat Angiotensin-converting enzyme 2 (ACE2) and, less favorably, human ACE2 for entry.
21 The two viruses use their spikes' S1 subunit carboxyl-terminal domains (S1-CTD) for high-affinity
22 and species-specific ACE2 binding. Cryo-electron microscopy analysis revealed a novel

23 coronavirus-ACE2 binding interface and a protein-glycan interaction, distinct from other known
24 ACE2-using viruses. We identified a molecular determinant close to the viral binding interface that
25 restricts human ACE2 from supporting NeoCoV infection, especially around residue Asp338.
26 Conversely, NeoCoV efficiently infects human ACE2 expressing cells after a T510F mutation on the
27 receptor-binding motif (RBM). Notably, the infection could not be cross-neutralized by antibodies
28 targeting SARS-CoV-2 or MERS-CoV. Our study demonstrates the first case of ACE2 usage in
29 MERS-related viruses, shedding light on a potential bio-safety threat of the human emergence of an
30 ACE2 using “MERS-CoV-2” with both high fatality and transmission rate.

31

32 **Keywords:** NeoCoV, PDF-2180-CoV, MERS-CoV, bat merbecovirus, ACE2, DPP4

33

34 **Introduction**

35 Coronaviruses (CoVs) are a large family of enveloped positive-strand RNA viruses classified into
36 four genera: Alpha-, Beta-, Gamma- and Delta-CoV. Generally, Alpha and Beta-CoV can infect
37 mammals such as bats and humans, while Gamma- and Delta-CoV mainly infect birds, occasionally
38 mammals⁶⁻⁸. It is thought that the origins of most coronaviruses infecting humans can be traced back
39 to their close relatives in bats, the most important animal reservoir of mammalian coronaviruses
40 ^{9,10}. Coronaviruses are well recognized for their recombination and host-jumping ability, which has
41 led to the three major outbreaks in the past two decades caused by SARS-CoV, MERS-CoV, and the
42 most recent SARS-CoV-2, respectively¹¹⁻¹⁴.

43 MERS-CoV belongs to the lineage C of Beta-CoV (Merbecoviruses), which poses a great threat
44 considering its high case-fatality rate of approximately 35%¹⁵. Merbecoviruses have also been found

45 in several animal species, including camels, hedgehogs, and bats. Although camels are confirmed
46 intermediate hosts of the MERS-CoV, bats, especially species in the family of *Vespertilionidae*, are
47 widely considered to be the evolutionary source of MERS-CoV or its immediate ancestor¹⁶.

48 Specific receptor recognition of coronaviruses is usually determined by the receptor-binding
49 domains (RBDs) on the carboxyl-terminus of the S1 subunit (S1-CTD) of the spike proteins¹⁷.
50 Among the four well-characterized coronavirus receptors, three are S1-CTD binding ectopeptidases,
51 including ACE2, DPP4, and aminopeptidase N (APN)^{1,18,19}. By contrast, the fourth receptor,
52 antigen-related cell adhesion molecule 1(CEACAM1a), interacts with the amino-terminal domain
53 (NTD) of the spike S1 subunit of the murine hepatitis virus^{20,21}. Interestingly, the same receptor can
54 be shared by distantly related coronaviruses with structurally distinct RBDs. For example, the
55 NL63-CoV (an alpha-CoV) uses ACE2 as an entry receptor widely used by many sarbecoviruses
56 (beta-CoV lineage B)²². A similar phenotype of cross-genera receptor usage has also been found in
57 APN, which is shared by many alpha-CoVs and a delta-CoV (PDCoV)⁷. In comparison, DPP4 usage
58 has only been found in merbecoviruses (beta-CoV lineage C) such as HKU4, HKU25, and related
59 strains²⁻⁴.

60 Intriguingly, many other merbecoviruses do not use DPP4 for entry and their receptor usage
61 remains elusive, such as bat coronaviruses NeoCoV, PDF-2180-CoV, HKU5-CoV, and hedgehog
62 coronaviruses EriCoV-HKU31^{5,23-25}. Among them, the NeoCoV, infecting *Neoromicia capensis* in
63 South Africa, represents a bat merbecovirus that happens to be the closest relative of MERS-CoV
64 (85% identity at the whole genome level)^{26,27}. PDF-2180-CoV, another coronavirus most closely
65 related to NeoCoV, infects *Pipistrellus hesperidus* native to Southwest Uganda^{23,28}. Indeed, NeoCoV
66 and PDF-2180-CoV share sufficient similarity with MERS-CoV across most of the genome,

67 rendering them taxonomically the same viral species^{27,29}. However, their S1 subunits are highly
68 divergent compared with MERS-CoV (around 43–45% amino acid similarity), in agreement with
69 their different receptor preference²³.

70 In this study, we unexpectedly found that NeoCoV and PDF-2180-CoV use bat ACE2 as their
71 functional receptor. The cryo-EM structure of NeoCoV RBD bound with the ACE2 protein
72 from *Pipistrellus pipistrellus* revealed a novel ACE2 interaction mode that is distinct from how
73 human ACE2 (hACE2) interacts with the RBDs from SARS-CoV-2 or NL63. Although NeoCoV
74 and PDF-2180-CoV cannot efficiently use hACE2 based on their current sequences, the spillover
75 events of this group of viruses should be closely monitored, considering their human emergence
76 potential after gaining fitness through antigenic drift.

77

78 **Results**

79 **Evidence of ACE2 usage**

80 To shed light on the relationship between merbecoviruses, especially NeoCoV and PDF-2180-CoV,
81 we conducted a phylogenetic analysis of the sequences of a list of human and animal coronaviruses.
82 Maximum likelihood phylogenetic reconstructions based on complete genome sequences showed
83 that NeoCoV and PDF-2180-CoV formed sister clade with MERS-CoV (Fig. 1a). In comparison, the
84 phylogenetic tree based on amino acid sequences of the S1 subunit demonstrated that NeoCoV and
85 PDF-2180-CoV showed a divergent relationship with MERS-CoV but are closely related to the
86 hedgehog coronaviruses (EriCoVs) (Fig. 1b). A sequence similarity plot analysis (Simplot) queried
87 by MERS-CoV highlighted a more divergent region encoding S1 for NeoCoV and PDF-2180-CoV
88 compared with HKU4-CoV (Fig. 1c). We first tested whether human DPP4 (hDPP4) could support

89 the infection of several merbecoviruses through a pseudovirus entry assay³⁰. The result revealed that
90 only MERS-CoV and HKU4-CoV showed significantly enhanced infection of 293T-hDPP4.
91 Unexpectedly, we detected a significant increase of entry of NeoCoV and PDF-2180-CoV in
92 293T-hACE2 but not 293T-hAPN, both of which are initially set up as negative controls ([Fig. 1d](#),
93 [Extended Data Fig.1](#)).

94 To further validate the possibility of more efficient usage of bat ACE2, we screened a bat ACE2
95 cell library individually expressing ACE2 orthologs from 46 species across the bat phylogeny, as
96 described in our previous study³¹([Extended Data Figs.2-3, Supplementary Table 1](#)). Interestingly,
97 NeoCoV and PDF-2180-CoV, but not HKU4-CoV or HKU5-CoV, showed efficient entry in cells
98 expressing ACE2 from most bat species belonging to *Vespertilionidae* (vesper bats). In contrast, no
99 entry or very limited entry in cells expressing ACE2 of humans or bats from the *Yinpterochiroptera*
100 group ([Fig. 1e-f, Extended Data Fig.4](#)). Consistent with the previous reports, the infection of
101 NeoCoV and PDF-2180-CoV could be remarkably enhanced by an exogenous trypsin
102 treatment²⁸([Extended Data Fig.5](#)). As indicated by the dual split protein (DSP)-based fusion assay³²,
103 Bat37ACE2 triggers more efficient cell-cell membrane fusion than hACE2 in the presence of
104 NeoCoV spike protein expression ([Fig. 1g-h](#)). Notably, the failure of the human or hedgehog ACE2
105 to support entry of EriCoV-HKU31 indicates that these viruses have a different receptor
106 usage ([Extended Data Fig.6](#)). In agreement with a previous study^{23,28}, our results against the
107 possibility that bat DPP4 act as a receptor for NeoCoV and PDF-2180-CoV, as none of the tested
108 DPP4 orthologs, from the vesper bats whose ACE2 are highly efficient in supporting viral entry,
109 could support a detectable entry of NeoCoV and PDF-2180-CoV ([Fig. 1i, Extended Data Fig.7](#)).
110 Infection assays were also conducted using several other cell types from different species, including

111 a bat cell line Tb 1 Lu, ectopically expressing ACE2 or DPP4 from Bat40 (*Antrozous pallidus*), and
112 each test yielded similar results ([Extended Data Fig.8](#)).

113

114 **S1-CTD mediated species-specific binding**

115 The inability of NeoCoV and PDF-2180-CoV to use DPP4 is consistent with their highly divergent
116 S1-CTD sequence compared with the MERS-CoV and HKU4-CoV. We produced S1-CTD-hFc
117 proteins (putative RBD fused to human IgG Fc domain) to verify whether their S1-CTDs are
118 responsible for ACE2 receptor binding. The live-cell binding assay based on cells expressing various
119 bat ACE2 showed a species-specific utilization pattern in agreement with the results of the
120 pseudovirus entry assays ([Fig. 2a](#)). The specific binding of several representative bat ACE2 was also
121 verified by flow-cytometry ([Fig. 2b](#)). We further determined the binding affinity by Bio-Layer
122 Interferometry (BLI) analysis. The results indicated that both viruses bind to the ACE2
123 from *Pipistrellus pipistrellus* (Bat37) with the highest affinity ($K_D=1.98\text{nM}$ for NeoCoV and 1.29nM
124 for PDF-2180-CoV). In contrast, their affinities for hACE2 were below the detection limit of our
125 BLI analysis ([Fig. 2c, Extended Data Fig.9](#)). An enzyme-linked immunosorbent assay (ELISA) also
126 demonstrated the strong binding between NeoCoV/PDF-2180-CoV S1-CTDs and Bat37ACE2, but
127 not hACE2 ([Fig. 2d](#)). Notably, as the ACE2 sequences of the hosts of NeoCoV and PDF-2180-CoV
128 are unknown, Bat37 represents the closest relative of the host of PDF-2180-CoV (*Pipisrellus*
129 *hesperidus*) in our study. The binding affinity was further verified by competitive neutralization
130 assays using soluble ACE2-ectodomain proteins or viral S1-CTD-hFc proteins. Again, the soluble
131 Bat37ACE2 showed the highest activity to neutralize viral infection caused by both viruses ([Fig.](#)
132 [2e-f](#)). Moreover, NeoCoV-S1-CTD-hFc could also potently neutralize NeoCoV and PDF-2180-CoV

133 infections of cells expressing Bat37ACE2 ([Fig. 2g](#)). We further demonstrated the pivotal role of
134 S1-CTD in receptor usage by constructing chimeric viruses and testing them for altered receptor
135 usage. As expected, batACE2 usage was changed to hDPP4 usage for a chimeric NeoCoV with CTD,
136 but not NTD, sequences replaced by its MERS-CoV counterpart ([Fig. 2h](#)). These results confirmed
137 that S1-CTD of NeoCoV and PDF-2180-CoV are RBDs for their species-specific interaction with
138 ACE2.

139

140 **Structural basis of ACE2 binding**

141 To unveil the molecular details of the virus-ACE2 binding, we then carried out structural
142 investigations of the Bat37ACE2 in complex with the NeoCoV and PDF-2180-CoV RBD. 3D
143 classification revealed that the NeoCoV-Bat37ACE2 complex primarily adopts a dimeric
144 configuration with two copies of ACE2 bound to two RBDs, whereas only a monomeric
145 conformation was observed in the PDF-2180-CoV-Bat37ACE2 complex ([Figs. 3a-b, Extended](#)
146 [Data Fig. 10-11](#)). We determined the structures of these two complexes at a resolution of 3.5 Å
147 and 3.8 Å, respectively, and performed local refinement to further improve the densities around the
148 binding interface, enabling reliable analysis of the interaction details ([Figs. 3a-b, Extended Data](#)
149 [Fig. 12-13 and Table 1-2](#)). Despite existing in different oligomeric states, the structures revealed
150 that both NeoCoV and PDF-2180-CoV recognized the Bat37ACE2 in a very similar way. We used
151 the NeoCoV-Bat37ACE2 structure for detailed analysis ([Figs. 3a-b and Extended Data Fig. 14](#)).
152 Like other structures of homologs, the NeoCoV RBD structure comprises a core subdomain
153 located far away from the engaging ACE2 and an external subdomain recognizing the receptor
154 ([Fig. 3c and Extended Data Fig. 15](#)). The external subdomain is a strand-enriched structure with

155 four anti-parallel β strands (β 6– β 9) and exposes a flat four-stranded sheet-tip for ACE2
156 engagement ([Fig. 3c](#)). By contrast, the MERS-CoV RBD recognizes the side surface of the DPP4
157 β -propeller via its four-stranded sheet-blade ([Fig. 3c](#)). The structural basis for the differences in
158 receptor usage can be inferred from two features: i) the local configuration of the four-stranded
159 sheet in the external domain of NeoCoV shows a conformational shift of η 3 and β 8 disrupting the
160 flat sheet-face for DPP4 binding and ii) relatively longer 6-7 and 8-9 loops observed in
161 MERS-CoV impair their binding in the shallow cavity of bat ACE2 ([Fig. 3c and Extended Data](#)
162 [Fig. 15](#)).

163 In the NeoCoV-Bat37ACE2 complex structure, relatively smaller surface areas (498 \AA^2 in
164 NeoCoV RBD and 439 \AA^2 in Bat37ACE2) are buried by the two binding entities compared to
165 their counterparts in the MERS-CoV-DPP4 complex (880 \AA^2 in MERS-CoV RBD and 812 \AA^2 in
166 DPP4; 956 \AA^2 in SARS-CoV-2 RBD and 893 \AA^2 in hACE2). The NeoCoV RBD inserts into an
167 apical depression constructed by α 11, α 12 helices and a loop connecting α 12 and β 4 of Bat37ACE2
168 through its four-stranded sheet tip ([Fig. 3d and Extended Data Table. 2](#)). Further examination of
169 the binding interface revealed a group of hydrophilic residues at the site, forming a network of
170 polar-contacts (H-bond and salt-bridge) network and hydrophobic interactions. These polar
171 interactions are predominantly mediated by the residues N504, N506, N511, K512, and R550
172 from the NeoCoV RBM and residues T53, E305, T334, D338, R340 from Bat37ACE2 ([Fig. 3d,](#)
173 [Extended Data Table. 2](#)). Notably, the methyl group from residues A509 and T510 of the NeoCoV
174 RBM are partially involved in forming a hydrophobic pocket with residues F308, W328, L333,
175 and I358 from Bat37ACE2 at the interface. A substitution of T510 with F in the PDF-2180-CoV
176 RBM further improves hydrophobic interactions, which is consistent with an increased binding

177 affinity observed for this point mutation (Figs. 3d, Extended Data Table. 2). Apart from
178 protein-protein contacts, the glycans of bat ACE2 at positions N54 and N329 sandwich the strands
179 (β 8– β 9), forming π - π interactions with W540 and hydrogen bonds with N532, G545, and R550
180 from the NeoCoV RBD, underpinning virus-receptor associations (Fig. 3d and Extended Data
181 Table. 2).

182 The critical residues were verified by introducing mutations and testing their effect on receptor
183 binding and viral entry. As expected, mutations N504F/N506F, N511Y, and R550N in the NeoCoV
184 RBD, abolishing the polar-contacts or introducing steric clashes, resulted in a significant reduction of
185 RBD binding and viral entry (Fig.3e-f). Similarly, E305K mutation in Bat37ACE2 eliminating the
186 salt-bridge also significantly impaired the receptor function. Moreover, the loss of function effect of
187 mutation N54A on Bat37ACE2 abolishing the N-glycosylation at residue 54 confirmed the
188 importance of the particular protein-glycan interaction in viral-receptor recognition. In comparison,
189 N329A abolishing the N-glycosylation at site N329, located far away from the binding interface, had
190 no significant effect on receptor function (Fig.3g-h).

191

192 Evaluation of zoonotic potential

193 A major concern is whether NeoCoV and PDF-2180-CoV could jump the species barrier and
194 infect humans. As mentioned above, NeoCoV and PDF-2180-CoV cannot efficiently interact with
195 human ACE2. Here we first examined the molecular determinants restricting hACE2 from
196 supporting the entry of these viruses. By comparing the binding interface of the other three
197 hACE2-using coronaviruses, we found that the SARS-CoV, SARS-CoV-2, and NL63 share similar
198 interaction regions that barely overlapped with the region engaged by NeoCoV (Fig. 4a). Analysis of

199 the overlapped binding interfaces reveals a commonly used hot spot around residues 329-330
200 ([Fig.4b](#)). Through sequences alignment and structural analysis of hACE2 and Bat37ACE2, we
201 predicted that the inefficient use of the hACE2 for entry by the viruses could be attributed to
202 incompatible residues located around the binding interfaces, especially the difference in sequences
203 between residues 337-342 ([Fig.4c](#)). We replaced these residues of hACE2 with those from the
204 Bat37ACE2 counterparts to test this hypothesis ([Fig.4c-d](#)). The substitution led to an approximately
205 15-fold and 30-fold increase in entry efficiency of NeoCoV and PDF-2180-CoV, respectively,
206 confirming that this region is critical for the determination of the host range. Further fine-grained
207 dissection revealed that N338 is the most crucial residue in restricting human receptor usage ([Fig.](#)
208 [4e-g](#)).

209 We further assessed the zoonotic potential of NeoCoV and PDF-2180-CoV by identifying the
210 molecular determinants of viral RBM, which might allow cross-species transmission through
211 engaging hACE2. After meticulously examining the critical residues based on the complex structures
212 and computational prediction tool mCSM-PPI³³([Fig. 4h, Extended Data Table. 4](#)), we predicted
213 increasing hydrophobicity around the residue T510 of NeoCoV might enhance the virus-receptor
214 interaction on hACE2 ([Fig. 4 i](#)). Interestingly, the PDF-2180-CoV already has an F511
215 (corresponding to site 510 of NeoCoV), which is consistent with its slightly higher affinity to human
216 ACE2 ([Extended Data Fig.16](#)). As expected, T510F substitutions in NeoCoV remarkably increased
217 its binding affinity with hACE2 ($K_D=16.9$ nM) and a significant gain of infectivity in 293T-hACE2
218 cells ([Fig. 4 j-k, Extended Data Fig.17-18](#)). However, PDF-2180-CoV showed much lower
219 efficiency in using hACE2 than NeoCoV-T510F, indicating other unfavorable residues are restricting
220 its efficient interaction with hACE2. Indeed, a G to A (corresponding to A509 in NeoCoV) mutation

221 in site 510, increasing the local hydrophobicity, partially restored its affinity to hACE2 ([Fig.4 j-k](#)). In
222 addition, the NeoCoV-T510F can enter the human colon cell line Caco-2 with much higher
223 efficiency than wild-type NeoCoV. It enters the Caco-2 exclusively through ACE2 as the infection
224 can be neutralized by an ACE2-targeting neutralizing antibody H11B11³⁴ ([Fig. 4l](#)). Humoral
225 immunity triggered by prior infection or vaccination of other coronaviruses might be inadequate to
226 protect humans from NeoCoV and PDF-2180-CoV infections because neither SARS-CoV-2 anti-sera
227 nor ten tested anti-MERS-CoV nanobodies can cross-inhibit the infection caused by these two
228 viruses³⁵. ([Fig. 4m-n](#)).

229

230 **Discussion:**

231 The lack of knowledge of the receptors of bat coronaviruses has greatly limited our understanding of
232 these high-risk pathogens. Our study provided evidence that the relatives of potential MERS-CoV
233 ancestors like NeoCoV and PDF-2180-CoV engage bat ACE2 for efficient cellular entry. However,
234 HKU5-CoV and EriCoV seem not to use bat DPP4 or hedgehog ACE2 for entry, highlighting the
235 complexity of coronaviruses receptor utilization. It was unexpected that NeoCoV and
236 PDF-2180-CoV use ACE2 rather than DPP4 as their entry receptors since their RBD core structures
237 resemble MERS-CoV more than other ACE2-using viruses ([Fig. 4a, Extended Data Fig. 15](#)).

238 Different receptor usage can affect the transmission rate of the viruses. Although it remains
239 unclear whether ACE2 usage out-weight DPP4 usage for more efficient transmission, MERS-CoV
240 appears to have lower transmissibility with an estimated R₀ around 0.69. Comparatively, the ACE2
241 usage has been approved able to achieve high transmissibility. The SARS-CoV-2 estimated R₀ is
242 around 2.5 for the original stain, 5.08 for the delta variant, and even higher for the omicron

243 variant³⁶⁻³⁸. This unexpected ACE2 usage of these MERS-CoV close relatives highlights a latent
244 biosafety risk, considering a combination of two potentially damaging features of high fatality
245 observed for MERS-CoV and the high transmission rate noted for SARS-CoV-2. Furthermore, our
246 studies show that the current COVID-19 vaccinations are inadequate to protect humans from any
247 eventuality of the infections caused by these viruses.

248 Many sarbecoviruses, alpha-CoV NL63, and a group of merbecoviruses reported in this study
249 share ACE2 for cellular entry. Our structural analysis indicates NeoCoV and PDF-2180-CoV bind to
250 an apical side surface of ACE2, which is different from the surface engaged by other ACE2-using
251 coronaviruses (Fig.4a). The interaction is featured by inter-molecular protein-glycan bonds formed
252 by the glycosylation at N54, which is not found in RBD-receptor interactions of other coronaviruses.
253 The different interaction modes of the three ACE2-using coronaviruses indicate a history of multiple
254 independent receptor acquisition events during evolution²². The evolutionary advantage of ACE2
255 usage in different CoVs remains enigmatic.

256 Our results support the previous hypothesis that the origin of MERS-CoV might be a result of
257 an intra-spike recombination event between a NeoCoV like virus and a DPP4-using virus²⁶. RNA
258 recombination can occur during the co-infection of different coronaviruses, giving rise to a new virus
259 with different receptor usage and host tropisms^{39,40}. It remains unclear whether the event took place
260 in bats or camels, and where the host switching happened. Although bat merbecoviruses are
261 geographically widespread, the two known ACE2-using merbecoviruses are inhabited in Africa.
262 Moreover, most camels in the Arabian Peninsula showing serological evidence of previous
263 MERS-CoV infection are imported from the Greater Horn of Africa with several Neoromicia
264 species⁴¹. Considering both viruses are inefficient in infecting human cells in their current form, the

265 acquisition of the hDPP4 binding domain would be a critical event driving the emergence of
266 MERS-CoV. Further studies will be necessary to obtain more evidence about the origin of
267 MERS-CoV.

268 The host range determinants on ACE2 are barriers for cross-species transmission of these
269 viruses. Our results show NeoCoV and PDF-2180-CoV favor ACE2 from bats of the
270 *Yangochiroptera* group, especially vesper bats (*Vespertilionidae*), where their host belongs to, but
271 not ACE2 orthologs from bats of the *Yinpterochiroptera* group. Interestingly, most merbecoviruses
272 were found in species belonging to the *Vespertilionidae* group, a highly diverse and widely
273 distributed family⁹. Although the two viruses could not use hACE2 efficiently, our study also reveals
274 that single residue substitution increasing local hydrophobicity around site 510 could enhance their
275 affinity for hACE2 and enable them to infect human cells expressing ACE2. Considering the
276 extensive mutations in the RBD regions of the SARS-CoV-2 variants, especially the heavily mutated
277 omicron variant, these viruses may hold a latent potential to infect humans through further adaptation
278 via antigenic drift^{42,43}. It is also very likely that their relatives with human emergence potential are
279 circulating somewhere in nature.

280 Overall, we identified ACE2 as a long-sought functional receptor of the potential MERS-CoV
281 ancestors in bats, facilitating the in-depth research of these important viruses with zoonotic
282 emergence risks. Our study adds to the knowledge about the complex receptor usage of
283 coronaviruses, highlighting the importance of surveillance and research on these viruses to prepare
284 for potential outbreaks in the future.

285

286 **Supplementary Information**

287

288 **Methods**

289 **Receptor and virus sequences.** The acquisition of sequences of 46 bat ACE2 and hACE were
290 described in our previous study³¹. The five bat DPP4 and hDPP4 sequences were directly retrieved
291 from the GenBank database (human DPP4, NM_001935.3; Bat37, Pipistrellus pipistrellus,
292 KC249974.1) or extracted from whole genome sequence assemblies of the bat species retrieved from
293 the GenBank database (Bat25, Sturnira hondurensis, GCA_014824575.2 ; Bat29, Mormoops
294 blainvillei , GCA_004026545.1; Bat36, Aeorestes cinereus, GCA_011751065.1; Bat40, Antrozous
295 pallidus, GCA_007922775.1). The whole genome sequences of different coronaviruses were
296 retrieved from the GenBank database. The accession numbers are as follows: MERS-CoV
297 (JX869059.2), Camel MERS-CoV KFU-HKU 19Dam (KJ650296.1), HKU4 (NC_009019.1), HKU5
298 (NC_009020.1), ErinaceusCoV/HKU31 strain F6 (MK907286.1), NeoCoV (KC869678.4),
299 PDF-2180-CoV (NC_034440.1), ErinaceusCoV/2012-174 (NC_039207.1), BtVs-BetaCoV/SC2013
300 (KJ473821.1), BatCoV/H.savii/Italy (MG596802.1), BatCoV HKU25 (KX442564.1), BatCoV
301 ZC45(MG772933.1) and SARS-CoV-2 (NC_045512.2), NL63 (JX504050.1) 229E (MT797634.1).
302 All gene sequences used in this study were commercially synthesized by Genewiz. The sources,
303 accession numbers, and sequences of the receptors and viruses were summarized in [Supplementary](#)
304 [Table 1](#).

305

306 **SARS-CoV-2 anti-sera collection.** All the vaccinated sera were collected from volunteers at about
307 21 days post the third dose of the WHO-approved inactivated SARS-COV-2 vaccine (CorovaVac,

308 Sinovac, China). All volunteers were provided informed written consent forms, and the whole study
309 was conducted following the requirements of Good Clinical Practice of China.

310

311 **Bioinformatic analysis.** Protein sequence alignment was performed using the MUSCLE algorithm
312 by MEGA-X software (version 10.1.8). For phylogenetic analysis, nucleotide or protein sequences of
313 the viruses were first aligned using the Clustal W and the MUSCLE algorithm, respectively. Then,
314 the phylogenetic trees were generated using the maximal likelihood method in MEGA-X (1000
315 Bootstraps). The model and the other parameters used for phylogenetic analysis were applied
316 following the recommendations after finding best DNA/Protein Models by the software. The
317 nucleotide similarity of coronaviruses was analyzed by SimPlot software (version 3.5.1) with a slide
318 windows size of 1000 nucleotides and a step size of 100 nucleotides using gap-stripped alignments
319 and the Kimura (2-parameter) distance model.

320

321 **Plasmids.** Human codon-optimized sequences of various ACE2 or DPP4 orthologs and their mutants
322 were cloned into a lentiviral transfer vector (pLVX-IRES-puro) with a C-terminal 3×Flag tag
323 (DYKDHD-G-DYKDHD-I-DYKDDDDK). The DNA sequences of human codon-optimized
324 NeoCoV S protein (AGY29650.2), PDF-2180-CoV S protein (YP_009361857.1), HKU4-CoV S
325 protein (YP_001039953.1), HKU5-CoV S protein (YP_001039962.1), HKU31 S protein
326 (QGA70692.1), SARS-CoV-2 (YP_009724390.1), and MERS-CoV S protein (YP_009047204.1)
327 were cloned into the pCAGGS vector with a C-terminal 13-15-amino acids deletion (corresponding
328 to 18 amino-acids in SARS-CoV-2) or replacement by an HA tag (YPYDVPDYA) for higher VSV
329 pseudotyping efficiency⁴⁴. The plasmids expressing coronavirus RBD-IgG-hFc fusion proteins were

330 generated by inserting the coding sequences of NeoCoV RBD (aa380-585), PDF-2180-CoV RBD
331 (aa381-586), HKU4-CoV (aa382-593), HKU5-CoV RBD (aa385-586), HKU31-CoV RBD
332 (aa366-575), SARS-CoV-2 RBD (aa331-524) and MERS-CoV RBD (aa377-588) into the pCAGGS
333 vector with an N-terminal CD5 secretion leading sequence (MPM GSLQPLATLYLLGMLVASVL).
334 The plasmids expressing soluble bat ACE2 and DPP4 proteins were constructed by inserting the
335 ectodomain coding sequences into the pCAGGS vector with N-terminal CD5 leader sequence and
336 C-terminal twin-strep tag and 3×Flag tag tandem sequences
337 (WSHPQFEKGGSGGGSGGSAAWSHPQFEK-GGGRS-DYKDHDGDYKDHDIDYKDDDDK).
338 Virus spike proteins or receptor-related mutants or chimeras were generated by overlapping PCR.
339 For Dual split protein (DSP) based cell-cell fusion assay, the dual reporter split proteins were
340 expressed by pLVX-IRES-puro vector expressing the RLuc_{aa1-155}-GFP_{1-7(aa1-157)} and
341 GFP_{8-11(aa158-231)}-RLuc-aa₁₅₆₋₃₁₁ plasmids, which were constructed in the lab based on a previously
342 study^{32,45}. The plasmids expressing the codon-optimized anti-ACE2 antibody (H11B11; GenBank
343 accession codes MZ514137 and MZ514138) were constructed by inserting the heavy-chain and
344 light-chain coding sequences into the pCAGGS vector with N-terminal CD5 leader sequences,
345 respectively³⁴. For anti-MERS-CoV nanobody-hFc fusion proteins, nanobody coding sequences were
346 synthesized and cloned into the pCAGGS vector with N-terminal CD5 leader sequences and
347 C-terminal hFc tags³⁵.

348

349 **Protein expression and purification.** The RBD-hFc (S1-CTD-hFc) fusion proteins of SARS-CoV-2,
350 MERS-CoV, HKU4-CoV, HKU5-CoV, HKU31-CoV, NeoCoV, and PDF-2180-CoV, and the
351 soluble ACE2 proteins of human, Bat25, Bat29, Bat36, Bat37, Bat38, and Bat40 were expressed by

352 293T by transfecting the corresponding plasmids by GeneTwin reagent (Biomed, TG101-01)
353 following the manufacturers' instructions. Four hrs post-transfection, the culture medium of the
354 transfected cells was replenished by SMM 293-TII Expression Medium (Sino Biological, M293TII).
355 The supernatant of the culture medium containing the proteins was collected every 2-3 days. The
356 recombinant RBD-hFc proteins were captured by Pierce Protein A/G Plus Agarose (Thermo
357 Scientific, 20424), washed by wash buffer W (100 mM Tris/HCl, pH 8.0, 150 mM NaCl, 1mM
358 EDTA), eluted with pH 3.0 Glycine buffer (100mM in H₂O), and then immediately balanced by
359 UltraPure 1M Tris-HCl, pH 8.0 (15568025, Thermo Scientific). The twin-strep tag containing
360 proteins were captured by Strep-Tactin XT 4Flow high capacity resin (IBA, 2-5030-002), washed by
361 buffer W, and eluted with buffer BXT (100 mM Tris/HCl, pH 8.0, 150 mM NaCl, 1mM EDTA,
362 50mM biotin). The eluted proteins can be concentrated and buffer-changed to PBS through
363 ultra-filtration. Protein concentrations were determined by Omni-Easy Instant BCA Protein Assay
364 Kit (Epizyme, ZJ102). The purified proteins were aliquoted and stored at -80°C. For Cryo-EM
365 analysis, NeoCoV RBD (aa380-588), PDF-2018-CoV RBD (381-589), and Bat37ACE2 (aa21-730)
366 were synthesized and subcloned into the vector pCAGGS with a C-terminal twin-strep tag. Briefly,
367 these proteins were expressed by transient transfection of 500 ml HEK Expi 293F cells (Gibco,
368 Thermo Fisher, A14527) using Polyethylenimine Max Mw 40,000 (polysciences). The resulting
369 protein samples were further purified by size-exclusion chromatography using a Superdex 75 10/300
370 Increase column (GE Healthcare) or a Superdex 200 10/300 Increase column (GE Healthcare) in
371 20mM HEPES, 100 mM NaCl, pH 7.5. For RBD-receptor complex (NeoCoV RBD-Bat37ACE2 /
372 PDF-2180-CoV RBD-Bat37ACE2), NeoCoV RBD or PDF-2180-CoV RBD was mixed with
373 Bat37ACE2 at the ratio of 1.2 :1, incubated for 30 mins on ice. The mixture was then subjected to

374 gel filtration chromatography. Fractions containing the complex were collected and concentrated to 2
375 mg/ml.

376

377 **Cell culture.** 293T (CRL-3216), VERO E6 cells (CRL-1586), A549 (CCL-185), BHK-21 (CCL-10),
378 and Huh-7 (PTA-4583), Caco2 (HTB-37) and the epithelial bat cell line Tb 1 Lu (CCL-88) were
379 purchased from American Type Culture Collection (ATCC) and cultured in Dulbecco's Modified
380 Eagle Medium, (DMEM, Monad, China) supplemented with 10% fetal bovine serum (FBS), 2.0 mM
381 of L-glutamine , 110 mg/L of sodium pyruvate and 4.5 g/L of D-glucose. An I1-Hybridoma
382 (CRL-2700) cell line secreting a neutralizing mouse monoclonal antibody against the VSV
383 glycoprotein (VSVG) was cultured in Minimum Essential Medium with Earles's balances salts and
384 2.0mM of L-glutamine (Gibico) and 10% FBS. All cells were cultures at 37°C in 5% CO₂ with the
385 regular passage of every 2-3 days. 293T stable cell lines overexpressing ACE2 or DPP4 orthologs
386 were maintained in a growth medium supplemented with 1 µg/ml of puromycin.

387

388 **Stable cell line generation.** Stable cell lines overexpressing ACE2 or DPP4 orthologs were
389 generated by lentivirus transduction and antibiotic selection. Specifically, the lentivirus carrying the
390 target gene was produced by cotransfection of lentiviral transfer vector (pLVX-EF1a-Puro, Genewiz)
391 and packaging plasmids pMD2G (Addgene, plasmid no.12259) and psPAX2 (Addgene, plasmid
392 no.12260) into 293T cells through Lip2000 Transfection Reagent (Biosharp, BL623B). The
393 lentivirus-containing supernatant was collected and pooled at 24 and 48 hrs post-transfection. 293T
394 cells were transduced by the lentivirus after 16 hrs in the presence of 8 µg/ml polybrene. Stable cells

395 were selected and maintained in the growth medium with puromycin (1-2 µg/ml). Cells selected for
396 at least ten days were considered stable cell lines and used in different experiments.

397

398 **Cryo-EM sample preparation and data collection.** For Cryo-EM sample preparation, the NeoCoV
399 RBD-Bat37ACE2 or PDF-2018-CoV RBD-Bat37ACE2 complex was diluted to 0.5 mg/ml.
400 Holy-carbon gold grid (Cflat R1.2/1.3 mesh 300) were freshly glow-discharged with a Solarus 950
401 plasma cleaner (Gatan) for 30s. A 3 µL aliquot of the mixture complex was transferred onto the grids,
402 blotted with filter paper at 16°C and 100% humidity, and plunged into the ethane using a Vitrobot
403 Mark IV (FEI). For these complexes, micrographs were collected at 300 kV using a Titan Krios
404 microscope (Thermo Fisher), equipped with a K2 detector (Gatan, Pleasanton, CA), using SerialEM
405 automated data collection software. Movies (32 frames, each 0.2 s, total dose 60^{e-Å⁻²}) were recorded
406 at a final pixel size of 0.82 Å with a defocus of between -1.2 and -2.0 µm.

407

408 **Image processing.** For NeoCoV RBD-Bat37ACE2 complex, a total of 4,234 micrographs were
409 recorded. For PDF-2018-CoV RBD-Bat37ACE2 complex, a total of 3,298 micrographs were
410 recorded. Both data sets were similarly processed. Firstly, the raw data were processed by
411 MotionCor2, which were aligned and averaged into motion-corrected summed images. Then, the
412 defocus value for each micrograph was determined using Gctf. Next, particles were picked and
413 extracted for two-dimensional alignment. The well-defined partial particles were selected for initial
414 model reconstruction in Relion⁴⁶. The initial model was used as a reference for three-dimensional
415 classification. After the refinement and post-processing, the overall resolution of PDF-2018-CoV
416 RBD-Bat37ACE2 complex was up to 3.8 Å based on the gold-standard Fourier shell correlation

417 (threshold = 0.143)⁴⁷. For the NeoCoV RBD-Bat37ACE2 complex, the C2 symmetry was expanded
418 before the 3D refinement. Finally, the resolution of the NeoCoV RBD-Bat37ACE2 complex was up
419 to 3.5Å. The quality of the local resolution was evaluated by ResMap⁴⁸.

420

421 **Model building and refinement.** The NeoCoV RBD-Bat37ACE2 complex structures were
422 manually built into the refined maps in COOT⁴⁷. The atomic models were further refined by
423 positional and B-factor refinement in real space using Phenix⁴⁸. For the PDF-2018-CoV
424 RBD-Bat37ACE2 complex model building, the refinement NeoCoV RBD-Bat37ACE2 complex
425 structures were manually docked into the refined maps using UCSF Chimera and further corrected
426 manually by real-space refinement in COOT. As the same, the atomic models were further refined by
427 using Phenix. Validation of the final model was performed with Molprobity⁴⁸. The data sets and
428 refinement statistics are shown in Extended Data table 1.

429

430 **Immunofluorescence assay.** The expression levels of ACE2 or DPP4 receptors were evaluated by
431 immunofluorescence assay detecting the C-terminal 3×FLAG-tags. The cells expressing the
432 receptors were seeded in the 96-well plate (poly-lysine pretreated plates for 293T based cells) at a
433 cell density of 1~5×10⁵/ml (100 µl per well) and cultured for 24 hrs. Cells were fixed with 100%
434 methanol at room temperature for 10 mins, and then incubated with a mouse monoclonal antibody
435 (M2) targeting the FLAG-tag (Sigma-Aldrich, F1804) diluted in 1% BSA/PBS at 37°C for 1 hour.
436 After one wash with PBS, cells were incubated with 2 µg/ml of the Alexa Fluor 594-conjugated goat
437 anti-mouse IgG (Thermo Fisher Scientific, A32742) diluted in 1% BSA/PBS at room temperature for

438 1 hour. The nucleus was stained blue with Hoechst 33342 (1:5,000 dilution in PBS). Images were
439 captured with a fluorescence microscope (Mshot, MI52-N).

440

441 **Pseudovirus production and titration.** Coronavirus spike protein pseudotyped viruses (CoV-psV)
442 were packaged according to a previously described protocol based on a replication-deficient
443 VSV-based rhabdoviral pseudotyping system (VSV-dG). The VSV-G glycoprotein-deficient VSV
444 coexpressing GFP and firefly luciferase (VSV-dG-GFP-fLuc) was rescued by a reverse genetics
445 system in the lab and helper plasmids from Karafast. For CoV-psV production, 293T or Vero E6
446 cells were transfected with the plasmids overexpressing the coronavirus spike proteins through the
447 Lip2000 Transfection Reagent (Biosharp, BL623B). After 36 hrs, the transfected cells were
448 transduced with VSV-dG-GFP-fLuc diluted in DMEM for 4 hrs at 37°C with a 50 % tissue culture
449 infectious dose (TCID₅₀) of 1×10^6 TCID₅₀/ml. Transduced cells were washed once with DMEM and
450 then incubated with culture medium and I1-hybridoma-cultured supernatant (1:10 dilution)
451 containing VSV neutralizing antibody to eliminate the infectivity of the residual input viruses. The
452 CoV-psV-containing supernatants were collected at 24 hrs after the medium change, clarified at
453 4,000 rpm for 5 mins, aliquoted, and stored at -80°C. The TCID₅₀ of pseudovirus was determined by
454 a serial-dilution based infection assay on 293T-bat40ACE2 cells for NeoCoV and PDF-2180-CoV or
455 293T-hDpp4 cells for MERS-CoV and HKU4-CoV. The TCID₅₀ was calculated according to the
456 Reed-Muench method ^{49,50}. The relative luminescence unit (RLU) value ≥ 1000 is considered
457 positive. The viral titer (genome equivalents) of HKU5-COV and HKU31-CoV without an ideal
458 infection system was determined by quantitative PCR with reverse transcription (RT-qPCR). The
459 RNA copies in the virus-containing supernatant were detected using primers in the VSV-L gene

460 sequences (VSV-L-F: 5'-TTCCGAGTTATGGGCCAGTT-3'; VSVL-R:
461 5'-TTGCCGTAGACCTCCAGT-3').

462

463

464 **Pseudovirus entry assay.** Cells for infection were trypsinized and incubated with different
465 pseudoviruses (1×10^5 TCID₅₀/well, or same genome equivalent) in a 96-well plate (5×10^4 /well) to
466 allow attachment and viral entry simultaneously. For TPCK-trypsin treatment for infection boosting,
467 NeoCoV and PDF-2180-CoV pseudovirus in serum-free DMEM were incubated with 100 µg/ml
468 TPCK-treated trypsin (Sigma-Aldrich, T8802) for 10 mins at 25°C, and then treated with 100 µg/ml
469 soybean trypsin inhibitor (Sigma-Aldrich, T6414) in DMEM+10% FBS to stop the proteolysis. At 16
470 hours post-infection (hpi), GFP images of infected cells were acquired with a fluorescence
471 microscope (Mshot, MI52-N), and intracellular luciferase activity was determined by a Bright-Glo
472 Luciferase Assay Kit (Promega, E2620) and measured with a SpectraMax iD3 Multi-well
473 Luminometer (Molecular Devices) or a GloMax 20/20 Luminometer (Promega).

474

475 **Pseudovirus neutralization Assay.** For antibody neutralization assays, the viruses (2×10^5
476 TCID₅₀/well) were incubated with the sera (50-fold diluted) or 10 µg/ml MERS-specific nanobodies
477 at 37°C for 30 mins, and then mixed with trypsinized BHK-21-Bat37ACE2 cells with the density of
478 2×10^4 /well. After 16 hrs, the medium of the infected cells was removed, and the cells were lysed
479 with 1×Bright-Glo Luciferase Assay reagent (Promega) for chemiluminescence detection with a
480 SpectraMax iD3 Multi-well Luminometer (Molecular devices).

481

482 **Western blot.** After one wash with PBS, the cells were lysed by 2% TritonX-100/PBS containing
483 1mM fresh prepared PMSF (Beyotime, ST506) on ice for 10 mins. Then cell lysate was clarified by
484 12,000 rpm centrifugation at 4°C for 5 mins, mixed with SDS loading buffer, and then incubated at
485 95 °C for 5 mins. After SDS-PAGE electrophoresis and PVDF membrane transfer, the membrane
486 was blocked with 5% skim milk/PBST at room temperature for one hour, incubated with primary
487 antibodies against Flag (Sigma, F1804), HA (MBL, M180-3), or glyceraldehyde-3-phosphate
488 dehydrogenase (GAPDH) (AntGene, ANT011) at 1:10000 dilution in 1% milk/PBS overnight on a
489 shaker at 4°C. After extensive wash, the membrane was incubated with the Horseradish peroxidase
490 (HRP)-conjugated secondary antibody AffiniPure Goat Anti-Mouse IgG (H+L) (Jackson Immuno
491 Research, 115-035-003) in 1% skim milk in PBST, and incubated for one hour. The blots were
492 visualized using Omni-ECL Femto Light Chemiluminescence Kit (EpiZyme, SQ201) by ChemiDoc
493 MP (Bio-Rad).

494

495 **Coronavirus RBD-hFc live-cell binding assay.** Recombinant coronavirus RBD-hFc proteins (1-16
496 μg/ml) were diluted in DMEM and then incubated with the cells for one hour at 37°C. Cells were
497 washed once with DMEM and then incubated with 2 μg/ml of Alexa Fluor 488-conjugated goat
498 anti-human IgG (Thermo Fisher Scientific; A11013) diluted in Hanks' Balanced Salt Solution
499 (HBSS) with 1% BSA for 1 hour at 37 °C. Cells were washed twice with PBS and incubated with
500 Hoechst 33342 (1:5,000 dilution in HBSS) for nucleus staining. Images were captured with a
501 fluorescence microscope (MI52-N). For flow cytometry analysis, cells were detached by 5mM of
502 EDTA/PBS and analyzed with a CytoFLEX Flow Cytometer (Beckman).

503

504 **Biolayer interferometry (BLI) binding assay.** The protein binding affinities were determined by
505 BLI assays performed on an Octet RED96 instrument (Molecular Devices). Briefly, 20 µg/mL
506 Human Fc-tagged RBD-hFc recombinant proteins were loaded onto a Protein A (ProA) biosensors
507 (ForteBio, 18-5010) for 30s. The loaded biosensors were then dipped into the kinetic buffer (PBST)
508 for 90s to wash out unbound RBD-hFc proteins. Subsequently, the biosensors were dipped into the
509 kinetic buffer containing soluble ACE2 with concentrations ranging from 0 to 500 nM for 120s to
510 record association kinetic and then dipped into kinetics buffer for 300s to record dissociation kinetics.
511 Kinetic buffer without ACE2 was used to define the background. The corresponding binding affinity
512 (K_D) was calculated with Octet Data Analysis software 12.2.0.20 using curve-fitting kinetic analysis
513 or steady-state analysis with global fitting.

514

515 **Enzyme-linked immunosorbent assay (ELISA).** To evaluate the binding between viral RBD and
516 the ACE2 *in vitro*, 96 well Immuno-plate were coated with ACE2 soluble proteins at 27 µg/ml in
517 BSA/PBS (100 µl/well) overnight at 4°C. After three wash by PBS containing 0.1% Tween-20
518 (PBST), the wells were blocked by 3% skim milk/PBS at 37°C for 2 hrs. Next, varying
519 concentrations of RBD-hFc proteins (1-9 µg/ml) diluted in 3% milk/PBST were added to the wells
520 and incubated for one hour at 37°C. After extensive wash, the wells were incubated with 1:2000
521 diluted HRP-conjugated goat anti-human Fc antibody (Sigma, T8802) in PBS for one hour. Finally,
522 the substrate solution (Solarbio, PR1210) was added to the plates, and the absorbance at 450nm was
523 measured with a SpectraMax iD3 Multi-well Luminometer (Molecular Devices).

524

525 **Cell-cell fusion assay**

526 Cell-cell fusion assay based on Dual Split proteins (DSP) was conducted on BHK-21 cells stably
527 expressing different receptors³². The cells were separately transfected with Spike and
528 RLuc_{aa1-155}-GFP_{1-10(aa1-157)} expressing plasmids, and Spike and GFP_{11(aa158-231)} RLuc-C_{aa156-311}
529 expressing plasmids, respectively. At 12 hrs after transfection, the cells were trypsinized and mixed
530 into a 96-well plate at 8×10⁴/well. At 26 hrs post-transfection, cells were washed by DMEM once
531 and then incubated with DMEM with or without 12.5 µg/ml TPCK-trypsin for 25 mins at RT. Five
532 hrs after treatment, the nucleus was stained blue with Hoechst 33342 (1:5,000 dilution in HBSS) for
533 30min at 37°C. GFP images were then captured with a fluorescence microscope (MI52-N; Mshot).
534 For live-cell luciferase assay, the EnduRen live cell substrate (Promega, E6481) was added to the
535 cells (a final concentration of 30 µM in DMEM) for at least 1 hour before detection by a GloMax
536 20/20 Luminometer (Promega).

537

538 **Statistical Analysis.**

539 Most experiments were repeated 2~5 times with 3-4 biological repeats, each yielding similar results.
540 Data are presented as MEAN±SD or MEAN±SEM as specified in the figure legends. All statistical
541 analyses were conducted using GraphPad Prism 8. Differences between independent samples were
542 evaluated by unpaired two-tailed t-tests; Differences between two related samples were evaluated by
543 paired two-tailed t-tests. P<0.05 was considered significant. * p<0.05, ** p <0.01, *** p <0.005, and
544 **** p <0.001.

545

546 **Acknowledgements**

547 We thank Dr. Xiaojun Huang, Dr. Xujing Li, and Dr. Lihong Chen for cryo-EM data collection at the
548 Center for Biological Imaging (CBI) in Institution of Biophysics, CAS. We thank Dr. Yuanyuan
549 Chen, Zhenwei Yang, Bingxue Zhou, and Xianjin Ou for technical support on BLI and SPR. We
550 thank professor Qihui Wang (Institute of Microbiology Chinese Academy of Sciences) for her
551 generous gift of Hedgehog ACE2 plasmid. We thank Ye Fu for his recommendations about
552 manuscript writing. We thank Beijing Taikang Yicai Foundation for their support to this work. This
553 study was supported by China NSFC projects (32070160); Fundamental Research Funds for the
554 Central Universities (2042020kf0024); Special Fund for COVID-19 Research of Wuhan University;
555 The Strategic Priority Research Program (XDB29010000, XDB37030000), CAS (YSBR-010);
556 National Key Research and Development Program (2020YFA0707500, 2018YFA0900801); Xiangxi
557 Wang was supported by Ten Thousand Talent Program and the NSFS Innovative Research Group
558 (No. 81921005).

559

560 **Author contributions**

561 H.Y. and X.X.W. conceived and designed the study. Q.X., L.C., C.B.M., C.L., J.Y.S., P.L., and F.T.
562 performed the experiments. Q.X., L.C., C.B.M., C.L., C.F.Z., H.Y., and X.X.W. analyzed the data. H.Y.,
563 X.X.W., Q.X., L.C., C.B.M., and C.L. interpreted the results. H.Y. and X.X.W. wrote the initial drafts of
564 the manuscript. H.Y., X.X.W., H.Y., X.X.W., L.C., and Q.X. revised the manuscript. C.B.M., C.L., P.
565 L., M.X.G., C.L.W., L.L.S., F.T., M.L.H., J.L., C.S., Y.C., H.B.Z., and K.L. commented on the
566 manuscript.

567

568 **Competing interests**

569 The authors declare no competing interests.

570

571 **Data availability**

572 The cryo-EM maps have been deposited at the Electron Microscopy Data Bank
573 (www.ebi.ac.uk/emdb) and are available under accession numbers: EMD-32686 (NeoCoV
574 RBD-Bat37ACE2 complex) and EMD-32693 (PDF-2180-CoV RBD-Bat37ACE2 complex). Atomic
575 models corresponding to EMD-32686, EMD-32693 have been deposited in the Protein Data Bank
576 (www.rcsb.org) and are available under accession numbers, PDB ID 7WPO, PDB ID 7WPZ,
577 respectively. The authors declare that all other data supporting the findings of this study are available
578 with the paper and its supplementary information files.

579

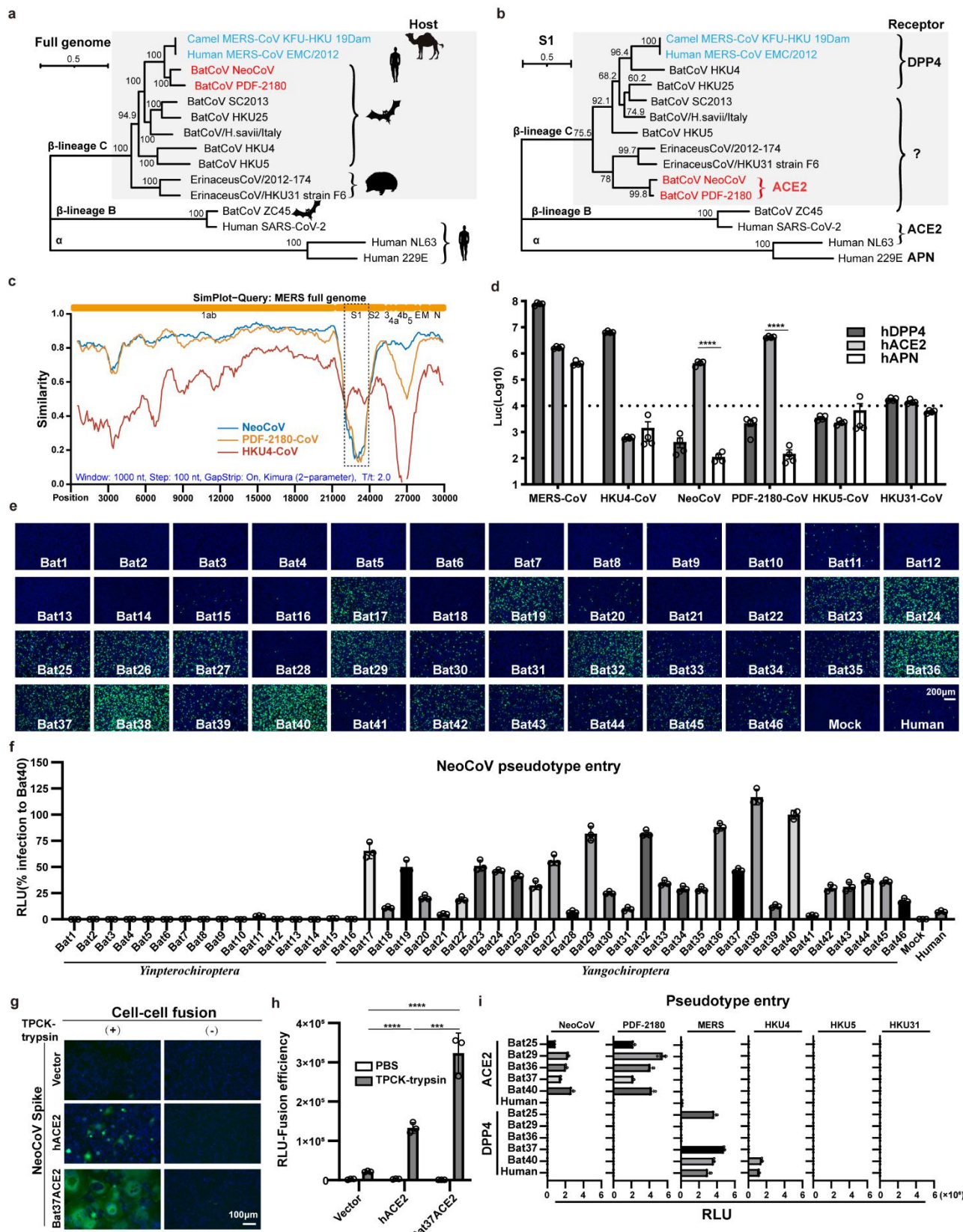
580

581 **Additional Information:**

582 Supplementary Information is available for this paper.

583 Correspondence and requests for materials should be addressed to H.Y. (huanyan@whu.edu.cn)

584



585

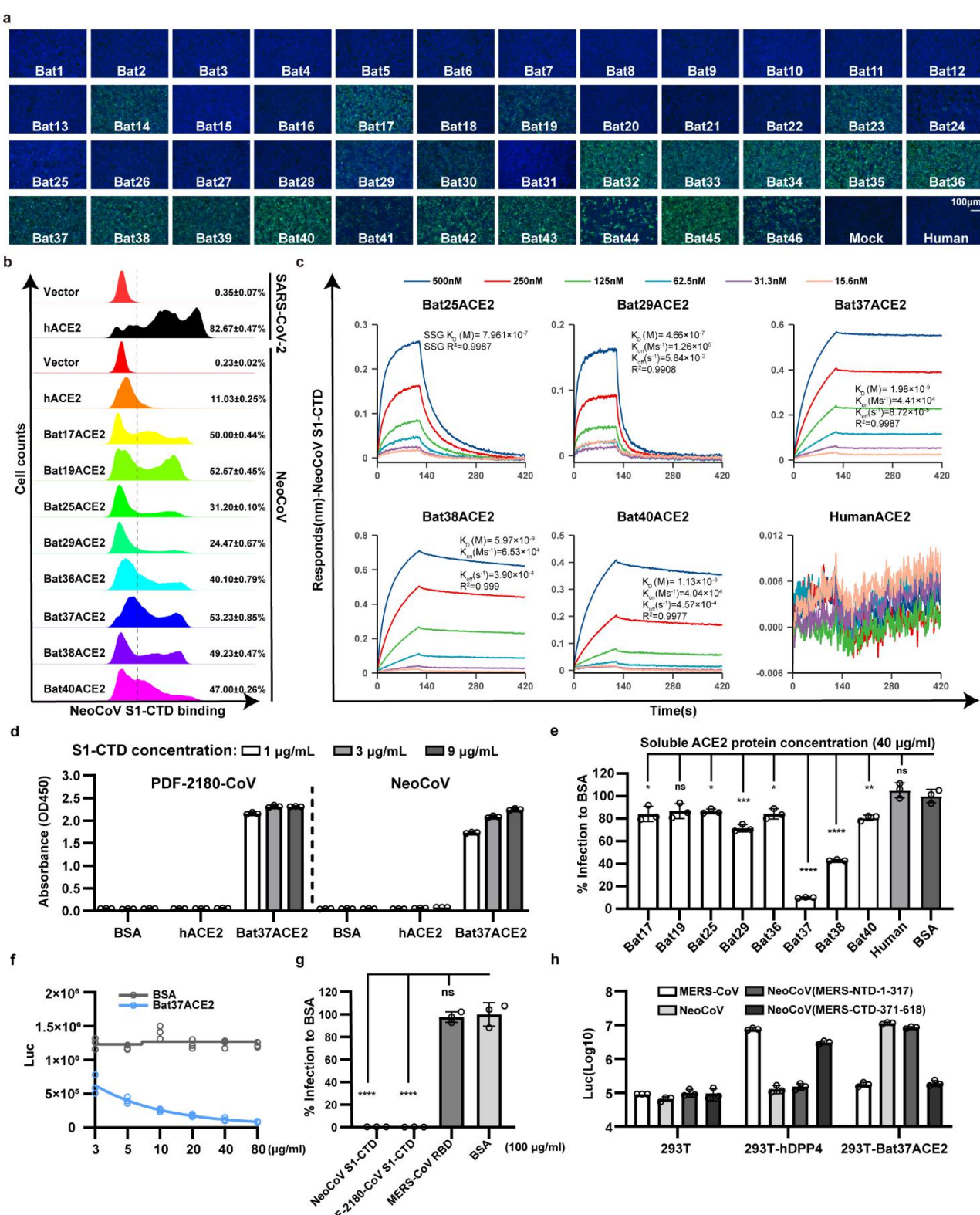
586 **Fig.1| A clade of bat merbecoviruses can use ACE2 but not DPP4 for efficient entry. a-b,**

587 Phylogenetical analysis of merbecoviruses (gray) based on whole genomic sequences (a) and S1

588 amino acid sequences (**b**). NL63 and 229E were set as outgroups. Hosts and receptor usage were
589 indicated. **c**, Simplot analysis showing the whole genome similarity of three merbecoviruses
590 compared with MERS-CoV. The regions that encode MERS-CoV proteins were indicated on the top.
591 Dashed box: S1 divergent region. **d**, Entry efficiency of six merbecoviruses in 293T cells stably
592 expressing hACE2, hDPP4, or hAPN. **e-f**, Entry efficiency of NeoCoV in cells expressing ACE2
593 from different bats. EGFP intensity (**e**); firefly luciferase activity (**f**). **g-h**, Cell-cell fusion assay
594 based on dual-split proteins showing the NeoCoV spike protein mediated fusion in BHK-21 cells
595 expressing indicated receptors. EGFP intensity (**g**), live-cell Renilla luciferase activity (**h**). **i**, Entry
596 efficiency of six merbecoviruses in 293T cells stably expressing the indicated bat ACE2 or DPP4.
597 Mean \pm SEM for **d, i**; Mean \pm SD for **f**, and **h**. (n=3). RLU: relative light unit.

598

599



600

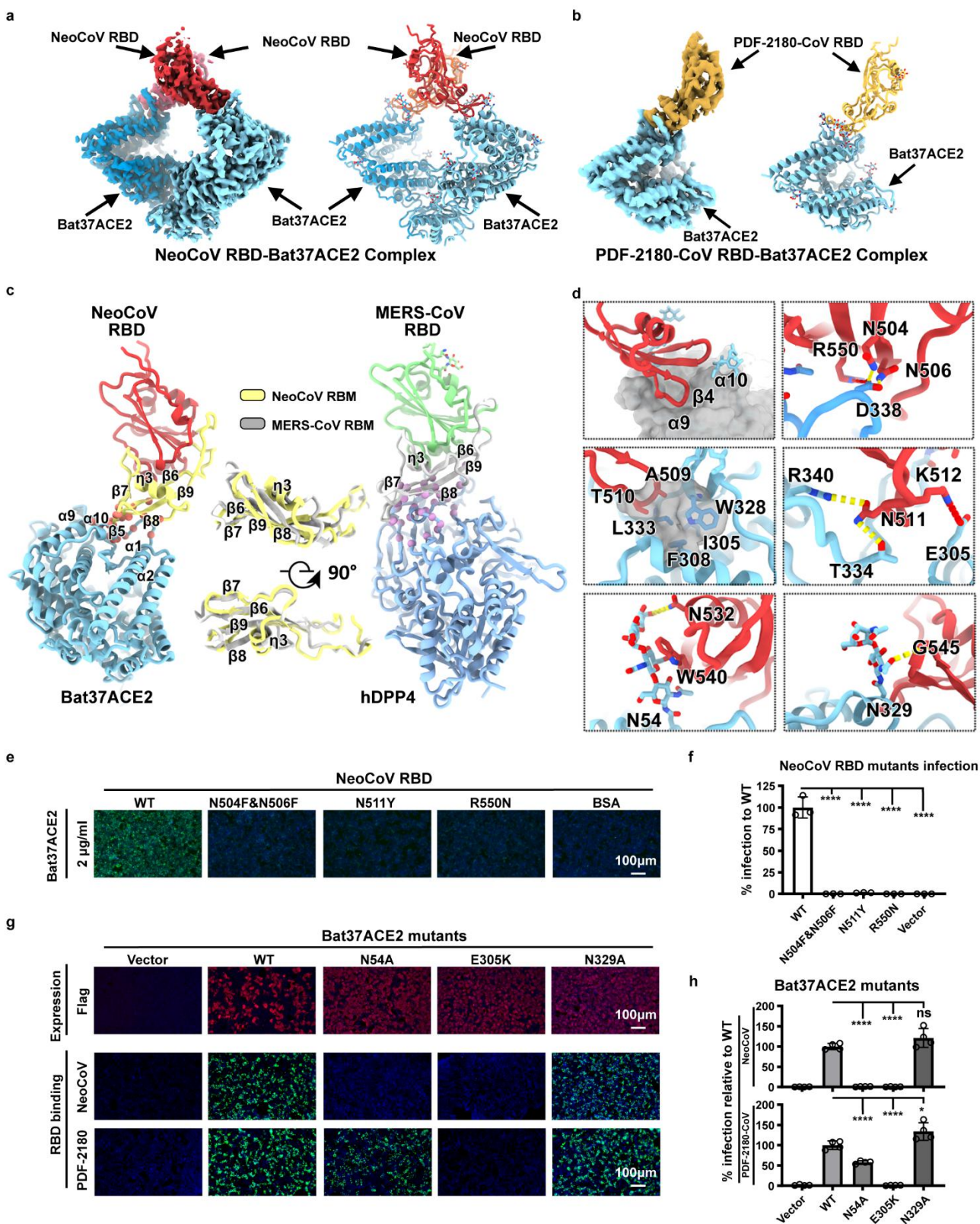
601 **Fig. 2| S1-CTD of NeoCoV and PDF-2180-CoV was required for species-specific ACE2 binding.**

602 **a**, Binding of NeoCoV-S1-CTD-hFc with 293T bat ACE2 cells via immunofluorescence detecting

603 the hFc. **b**, Flow cytometry analysis of NeoCoV-S1-CTD-hFc binding with 293T cells expressing the

604 indicated ACE2. The positive ratio was indicated based on the threshold (dash line). **c**, BLI assays
605 analyzing the binding kinetics between NeoCoV-S1-CTD-hFc with selected ACE2-ecto proteins. **d**,
606 ELISA assay showing the binding efficiency of NeoCoV and PDF-2180-CoV S1-CTD to human and
607 Bat37ACE2-ecto proteins. **e**, The inhibitory activity of soluble ACE2-ecto proteins against NeoCoV
608 infection in 293T-Bat37ACE2. **f**, Dose-dependent competition of NeoCoV infection by
609 Bat37ACE2-ecto proteins in 293T-Bat37ACE2 cells. **g**, The inhibitory effect of NeoCoV,
610 PDF-2180-CoV S1-CTD-hFc and MERS-CoV RBD-hFC proteins on NeoCoV infection in
611 293T-Bat37ACE2 cells. **h**, Receptor preference of chimeric viruses with S1-CTD or S1-NTD swap
612 mutations in cells expressing the indicated receptors. Mean±SD for **d**, **e**, **g**, and **h**, (n=3).

613

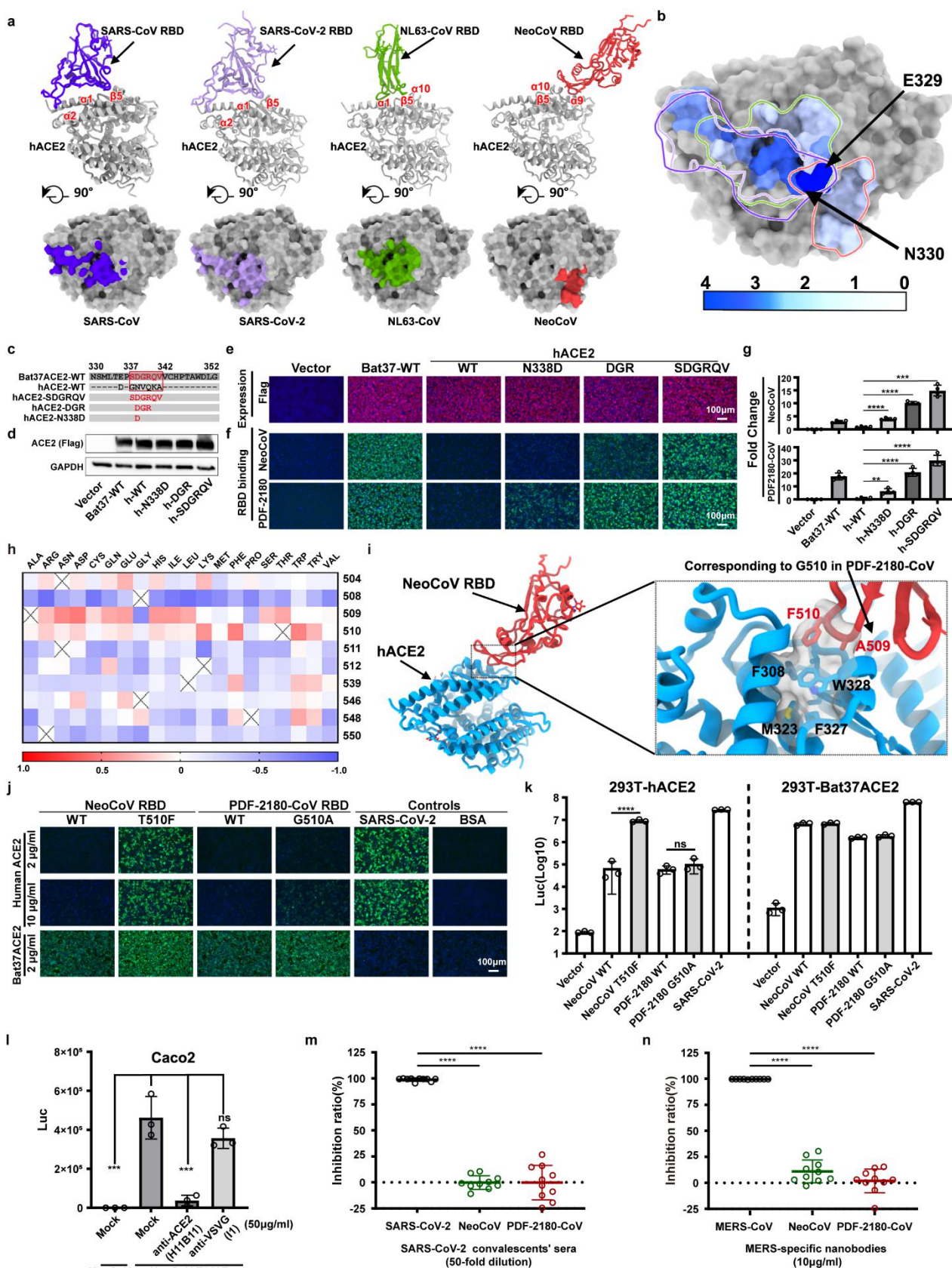


614

615 **Fig. 3| Structure of the NeoCoV RBD-Bat37ACE2 and PDF-2018-CoV RBD-Bat37ACE2**
616 **complex. a-b,** Cryo-EM density map and cartoon representation of NeoCoV RBD-Bat37ACE2

617 complex (**a**) and PDF-2018CoV RBD-Bat37ACE2 complex (**b**). The NeoCoV RBD,
618 PDF-2180-CoV RBD, and Bat37ACE2 were colored by red, yellow, and cyan, respectively. **c**,
619 Structure comparison between NeoCoV RBD-Bat37ACE2 complex (left) and MERS-CoV
620 RBD-hDPP4 complex (right). The NeoCoV RBD, MERS-CoV RBD, NeoCoV RBM, MERS-CoV
621 RBM, Bat37ACE2, and hDPP4 were colored in red, light green, light yellow, gray, cyan, and blue,
622 respectively. **d**, Details of the NeoCOV RBD-Bat37ACE2 complex interface. All structures are
623 shown as ribbon with the key residues shown with sticks. The salt bridges and hydrogen bonds are
624 presented as red and yellow dashed lines, respectively. **e-f**, Verification of the critical residues on
625 NeoCoV RBD affecting viral binding (**e**), and entry efficiency (**f**) in 293T-Bat37ACE2 cells. **g-h**,
626 Verification of the critical residues on Bat37ACE2 affecting NeoCoV RBD binding (**g**), and viral
627 entry efficiency(**h**). Mean \pm SD for **f** (n=3) and **h** (n=4).

628



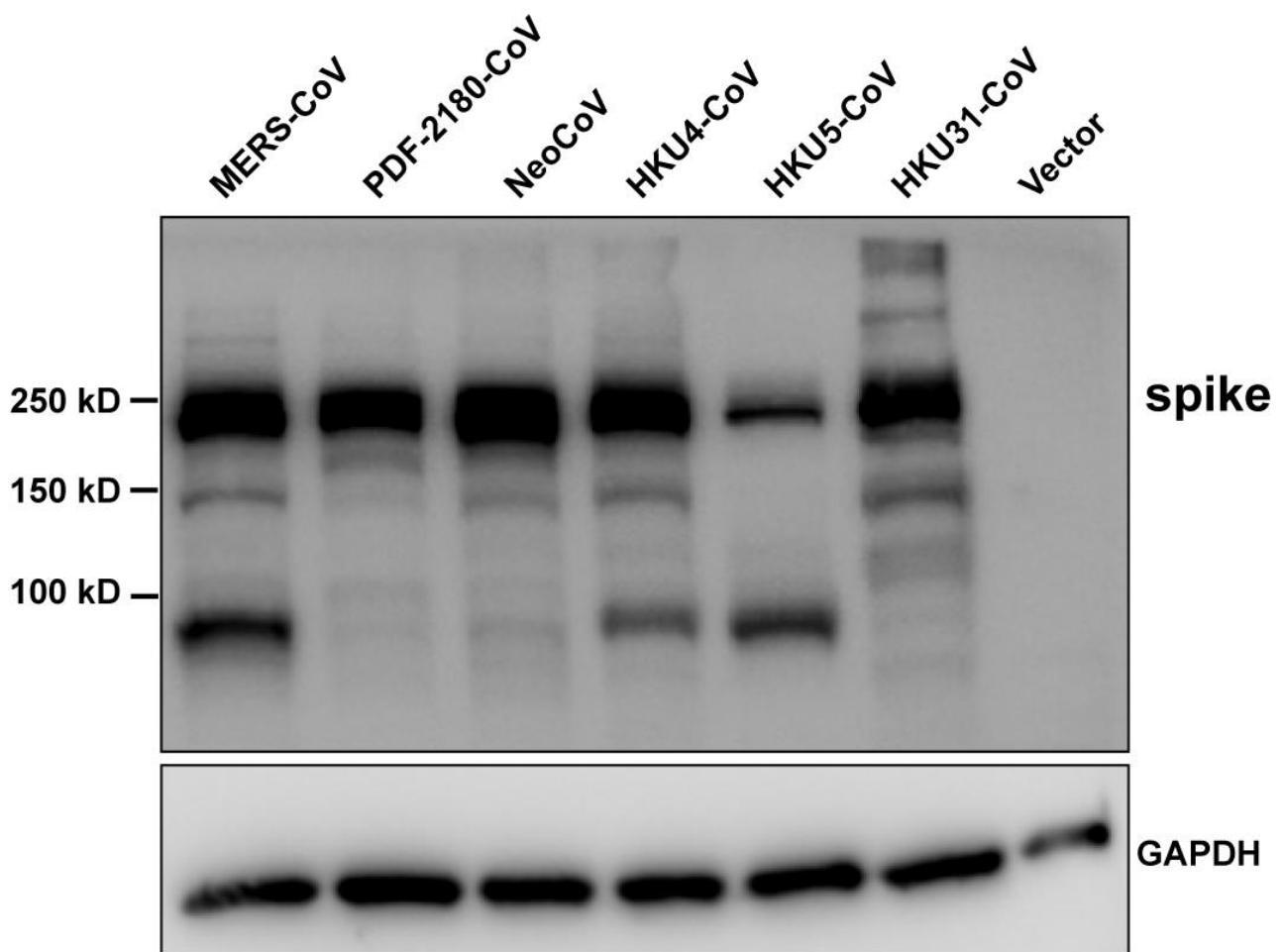
629

Fig. 4| Molecular determinants affecting hACE2 recognition by the viruses. **a**, Binding modes of ACE2-adapted coronaviruses. The SARS-CoV RBD, SARS-CoV-2 RBD, NL63-CoV RBD, and

632 NeoCoV RBD were colored in purple, light purple, green, and red, respectively. **b**, A common
633 virus-binding hot spot on ACE2 for the four viruses. Per residue frequency recognized by the
634 coronavirus RBDs were calculated and shown. **c**, Schematic illustration of the hACE2 swap mutants
635 with Bat37ACE2 counterparts. **d-e**, The expression level of the hACE2 mutants by Western blot (**d**)
636 and immunofluorescence (**e**). **f-g**, Receptor function of hACE2 mutants evaluated by virus RBD
637 binding assay (**f**) and pseudovirus entry assay (**g**). **h**, Molecular dynamics (MD) analysis of the effect
638 of critical residue variations on the interaction between NeoCoV and Bat37ACE2 by mCSM-PPI2. **i**,
639 Structure of NeoCoV RBD-hACE2 complex modeling by superposition in COOT. The NeoCoV
640 RBD and hACE2 were colored in red and sky blue, respectively. Details of the NeoCoV RBD key
641 mutation T510F was shown. All structures are presented as ribbon with the key residues shown with
642 sticks. **j-k**, The effect of NeoCoV and PDF-2180-CoV RBM mutations on hACE2 fitness as
643 demonstrated by binding (**j**) and entry efficiency (**k**) on 293T-hACE2 and 293T-Bat37ACE2 cells. **l**,
644 hACE2 dependent entry of NeoCoV-T510F in Caco2 cells in the presence of 50µg/ml of Anti-ACE2
645 (H11B11) or Anti-VSVG (I1). **m**, Neutralizing activity of SARS-CoV-2 vaccinated sera against the
646 infection by SARS-CoV-2, NeoCoV, and PDF-2180-CoV. **n**, Neutralizing activity of MERS-RBD
647 targeting nanobodies against the infections by MERS-CoV, NeoCoV, and PDF-2180-CoV. Mean ±
648 SD for **g,k-n**; **g(n=4),k-l (n=3)**, **gm-n (n=10)**.
649

650 **Extended Data Figures**

651

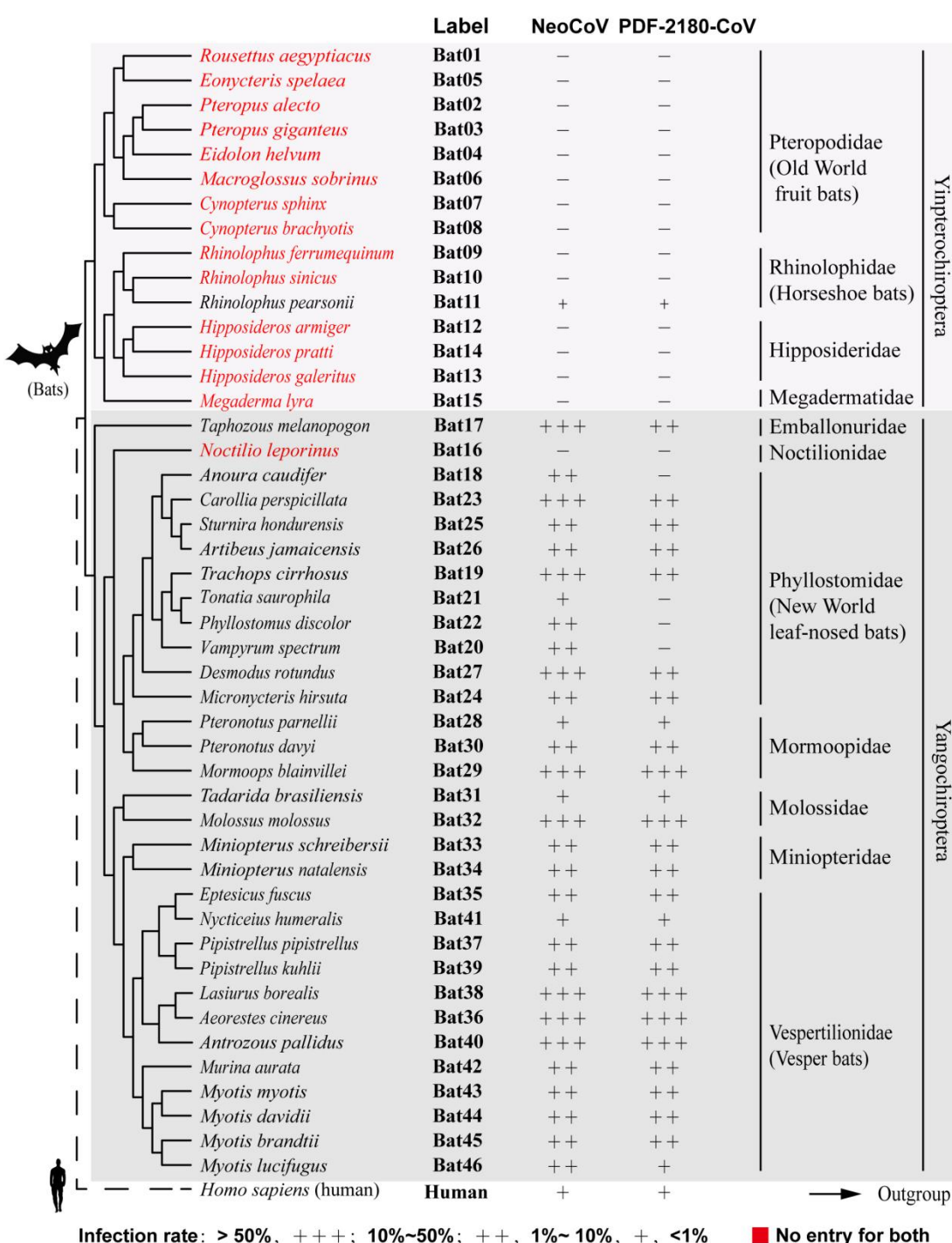


652

653 **Extended Data Figure 1 | Expression level of coronaviruses spike proteins used for**
654 **pseudotyping.**

655

656



657

658

659 Extended Data Figure 2 | Receptor function of ACE2 from 46 bat species in supporting

660 NeoCoV and PDF-2180-CoV entry.

661

662

Bat1	Bat2	Bat3	Bat4	Bat5	Bat6	Bat7	Bat8	Bat9	Bat10	Bat11	Bat12
Bat13	Bat14	Bat15	Bat16	Bat17	Bat18	Bat19	Bat20	Bat21	Bat22	Bat23	Bat24
Bat25	Bat26	Bat27	Bat28	Bat29	Bat30	Bat31	Bat32	Bat33	Bat34	Bat35	Bat36
Bat37	Bat38	Bat39	Bat40	Bat41	Bat42	Bat43	Bat44	Bat45	Bat46	Mock	Human

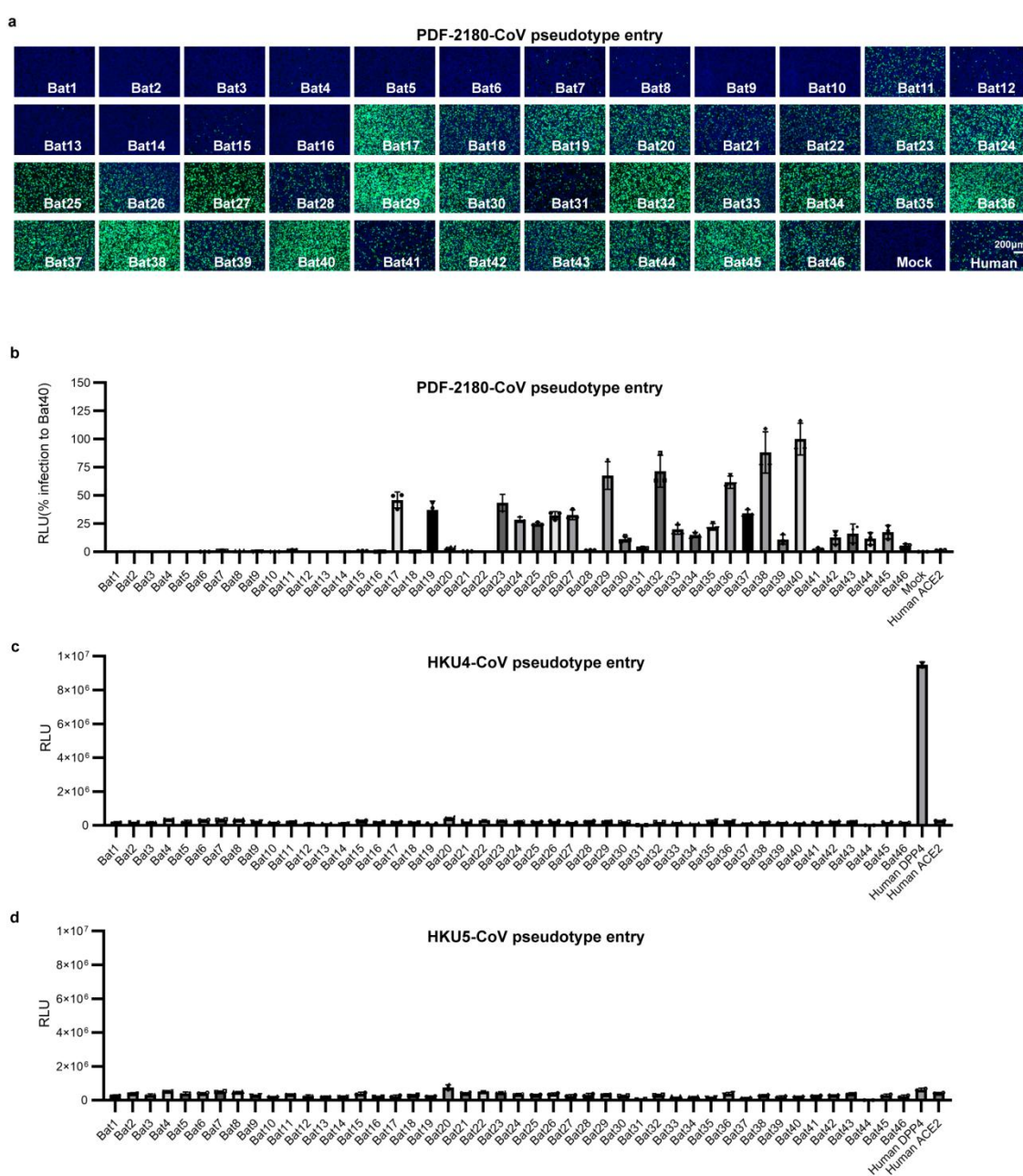
663

664

665 **Extended Data Figure 3 | The expression level of 46 bat ACE2 orthologs in 293T cells as**
666 **indicated by immunofluorescence assay detecting the C-terminal 3×FLAG Tag.**

667

668

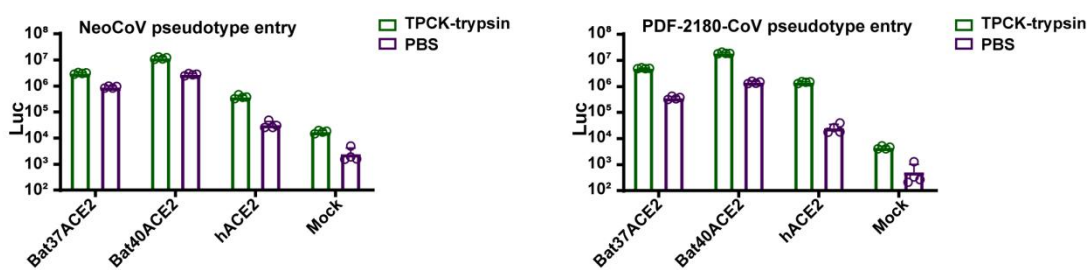


669

670 Extended Data Figure 4 | Entry efficiency of PDF-2180-CoV (a-b), HKU4-CoV (c), and
671 HKU5-CoV (d) pseudoviruses in 293T cells expressing different bat ACE2 orthologs

672

673

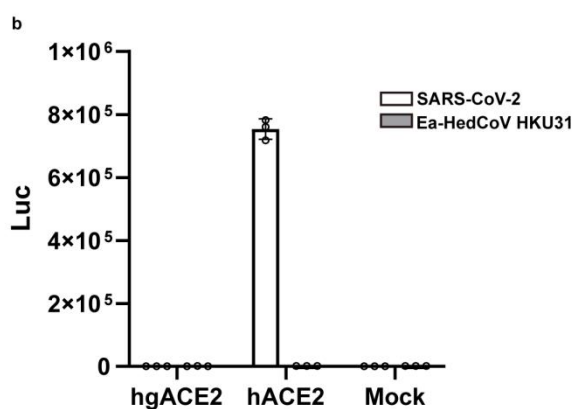
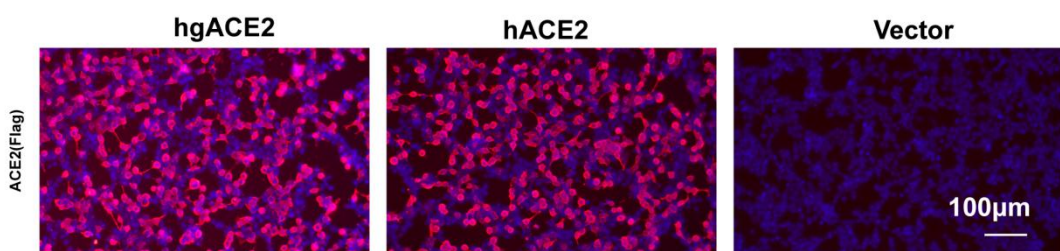


674

675 **Extended Data Figure 5 | TPCK-trypsin treatment significantly boosted the entry efficiency of**
676 **NeoCoV and PDF-2180-CoV on 293T cells expressing different ACE2 orthologs.**

677

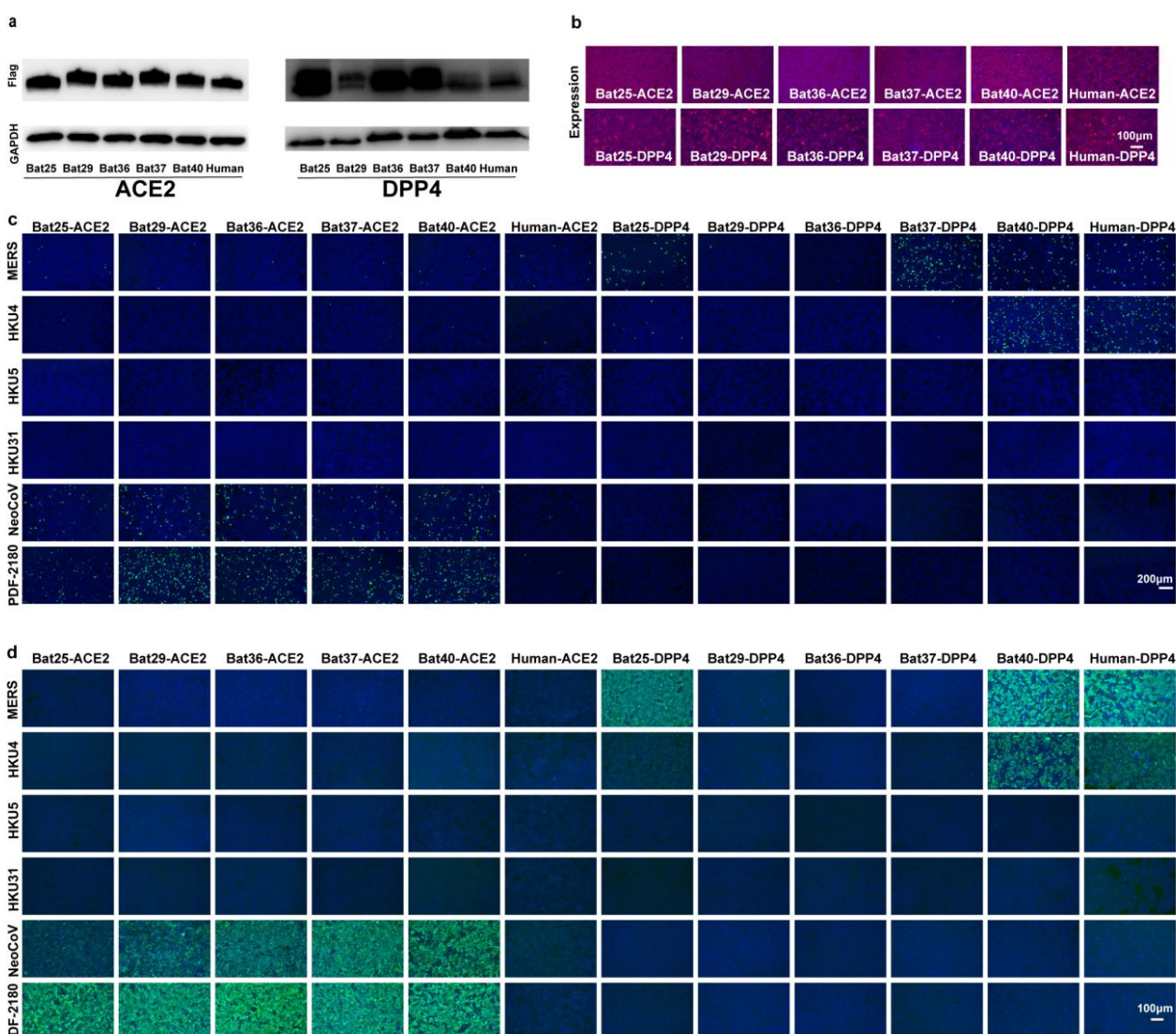
678



679

680 **Extended Data Figure 6 | Hedgehog ACE2 (hgACE2) cannot support the entry of**
681 **Ea-HedCoV-HKU31.** (a) The expression level of ACE2 was evaluated by immunofluorescence
682 detecting the C-terminal fused Flag tag. (b) Viral entry of SARS-CoV-2 and HKU31 into cells
683 expressing hACE2 or hgACE2.

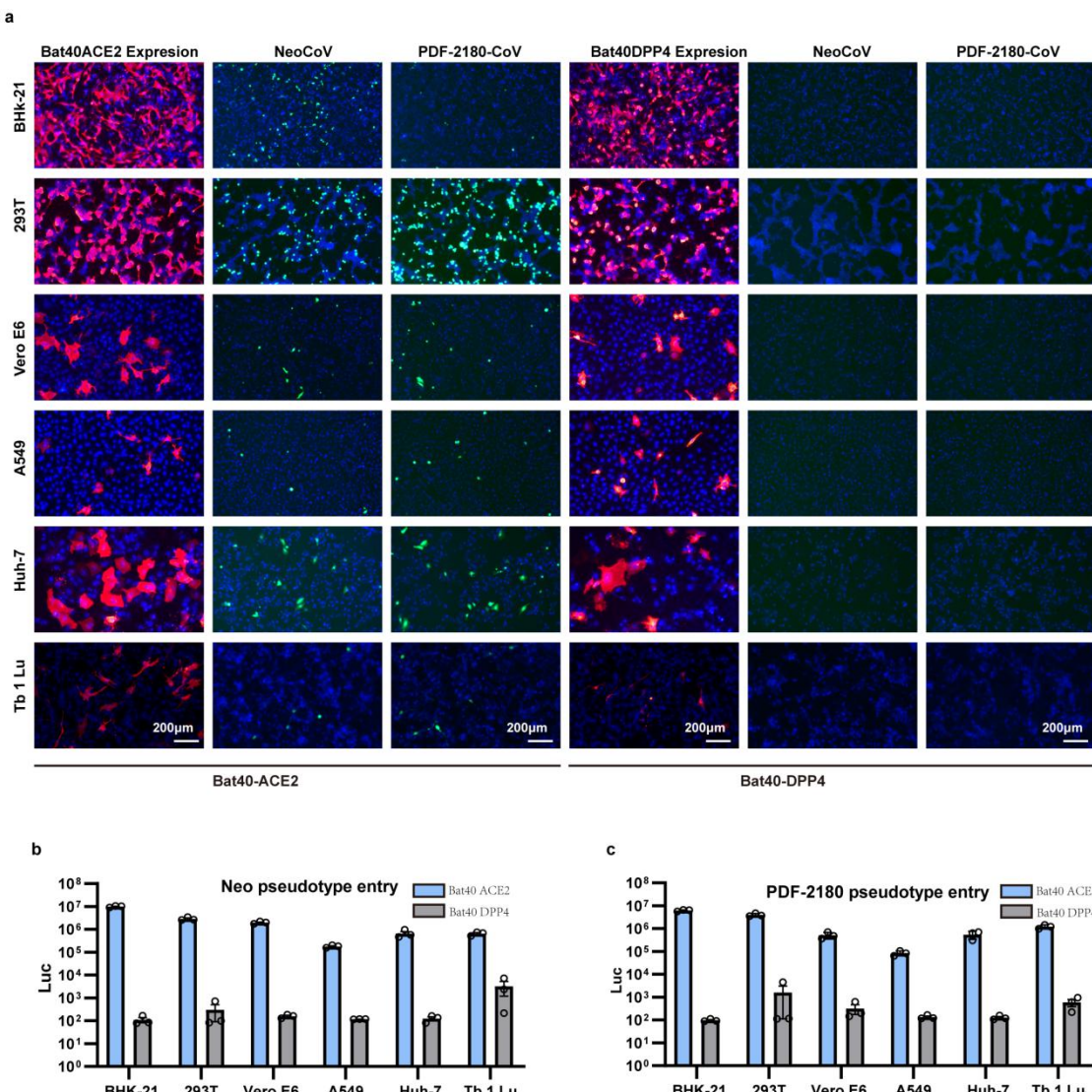
684



685

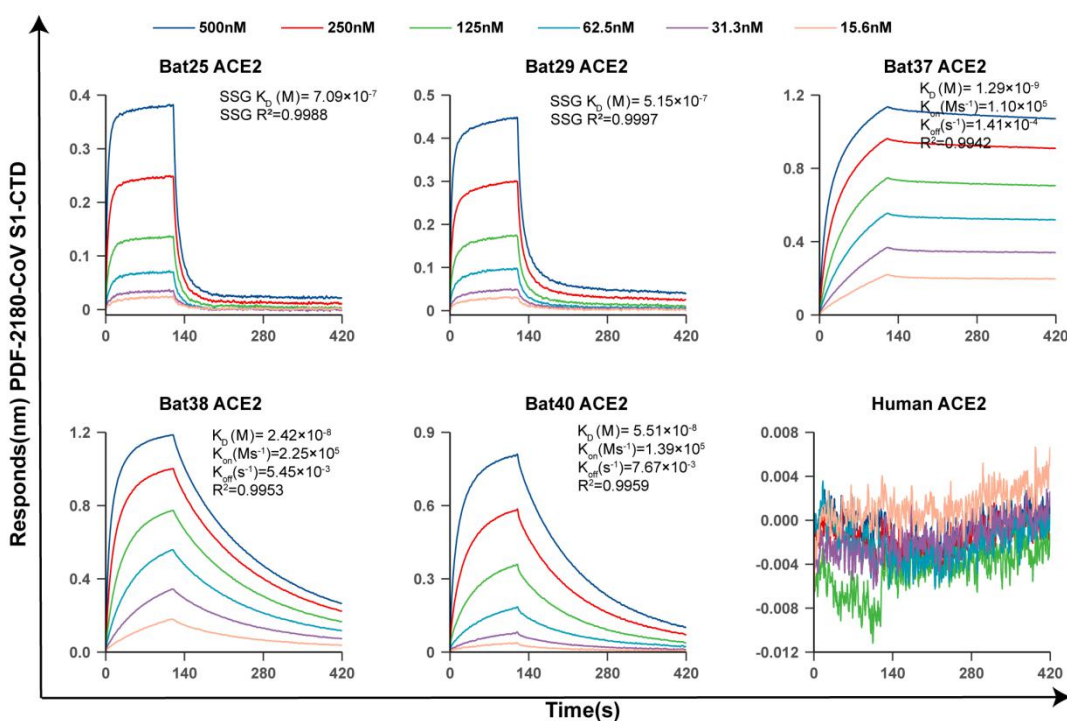
686 **Extended Data Figure 7 | ACE2 and DPP4 receptor usage of different merbecoviruses. a,**
687 Western blot detected the expression levels of ACE2 and DPP4 orthologs in 293T cells.**b,** The
688 intracellular bat ACE2 expression level by immunofluorescence assay detecting the C-terminal
689 3×FLAG-tag. **c-d,** Viral entry (**c**) and RBD binding (**d**) of different coronaviruses on 293T cells
690 expressing different ACE2 and DPP4 orthologs.

691



692

693 Extended data Figure 8 | NeoCoV and PDF2180-CoV infection of different cell types
694 expressing either Bat40ACE2 or Bat40DPP4. The BHK-21, 293T, Vero E6, A549, Huh-7, and Tb
695 1 Lu were transfected with either Bat40ACE2 or Bat40DPP4. The expression and viral entry (GFP)
696 (a) and luciferase activity (c) were detected at 16 hpi.

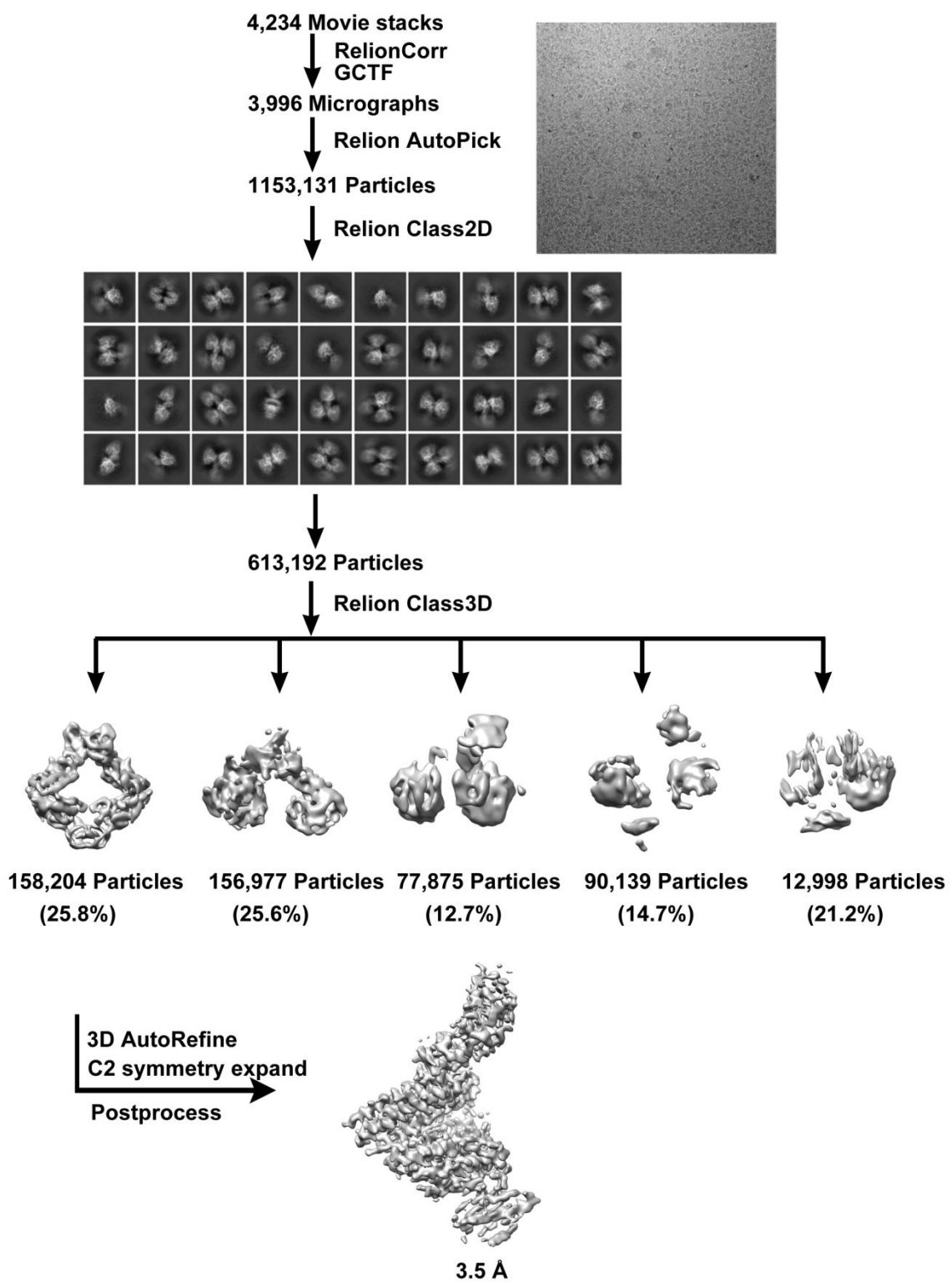


698

699 **Extended data Figure 9 | BLI analysis of the binding kinetics of PDF-2180-CoV S1-CTD**

700 **interacting with different ACE2 orthologs.**

701

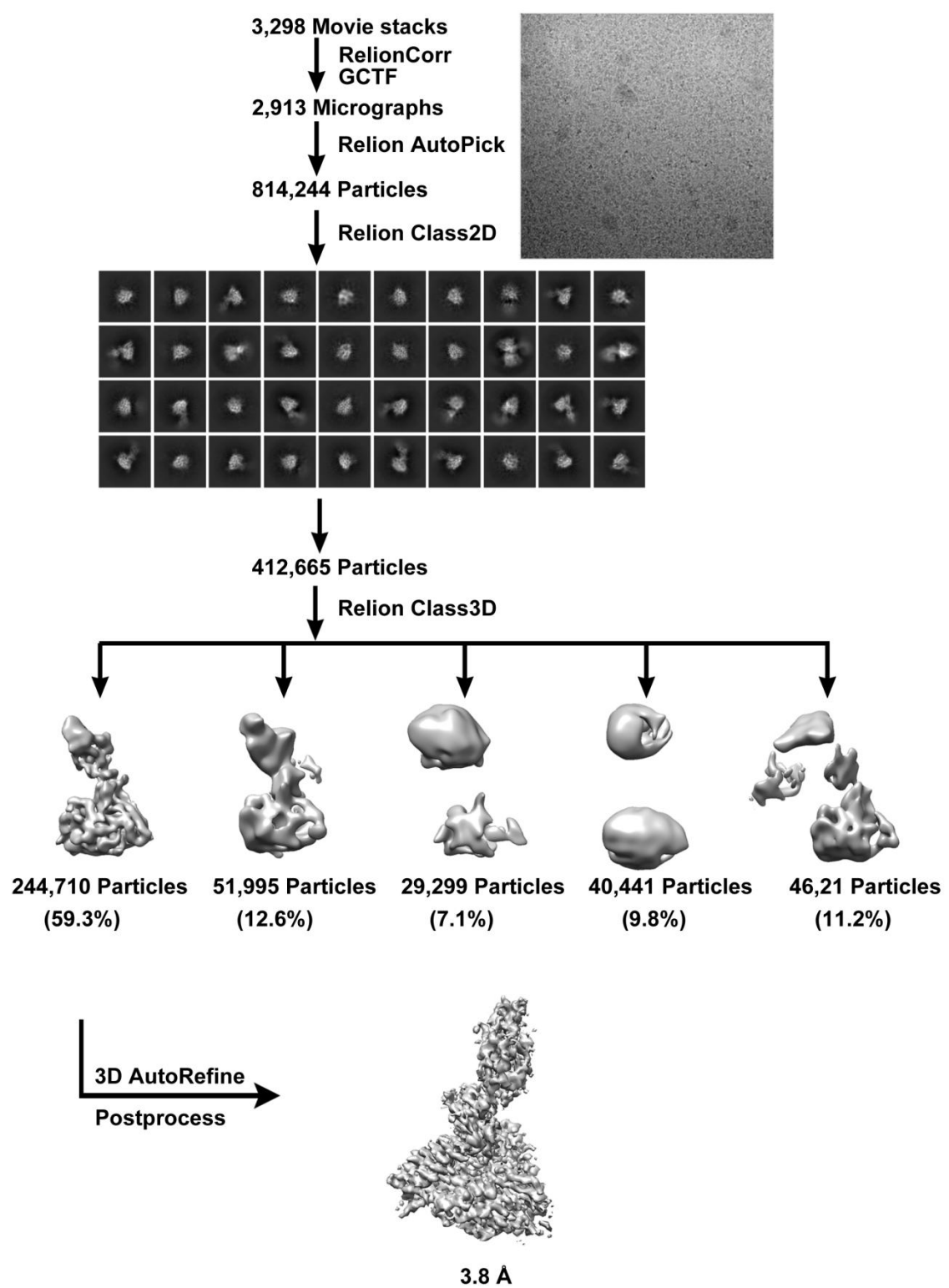


702

703 Extended data Figure 10 | Flowcharts for cryo-EM data processing of Neo-CoV

704 RBD-Bat37ACE2 complex.

705

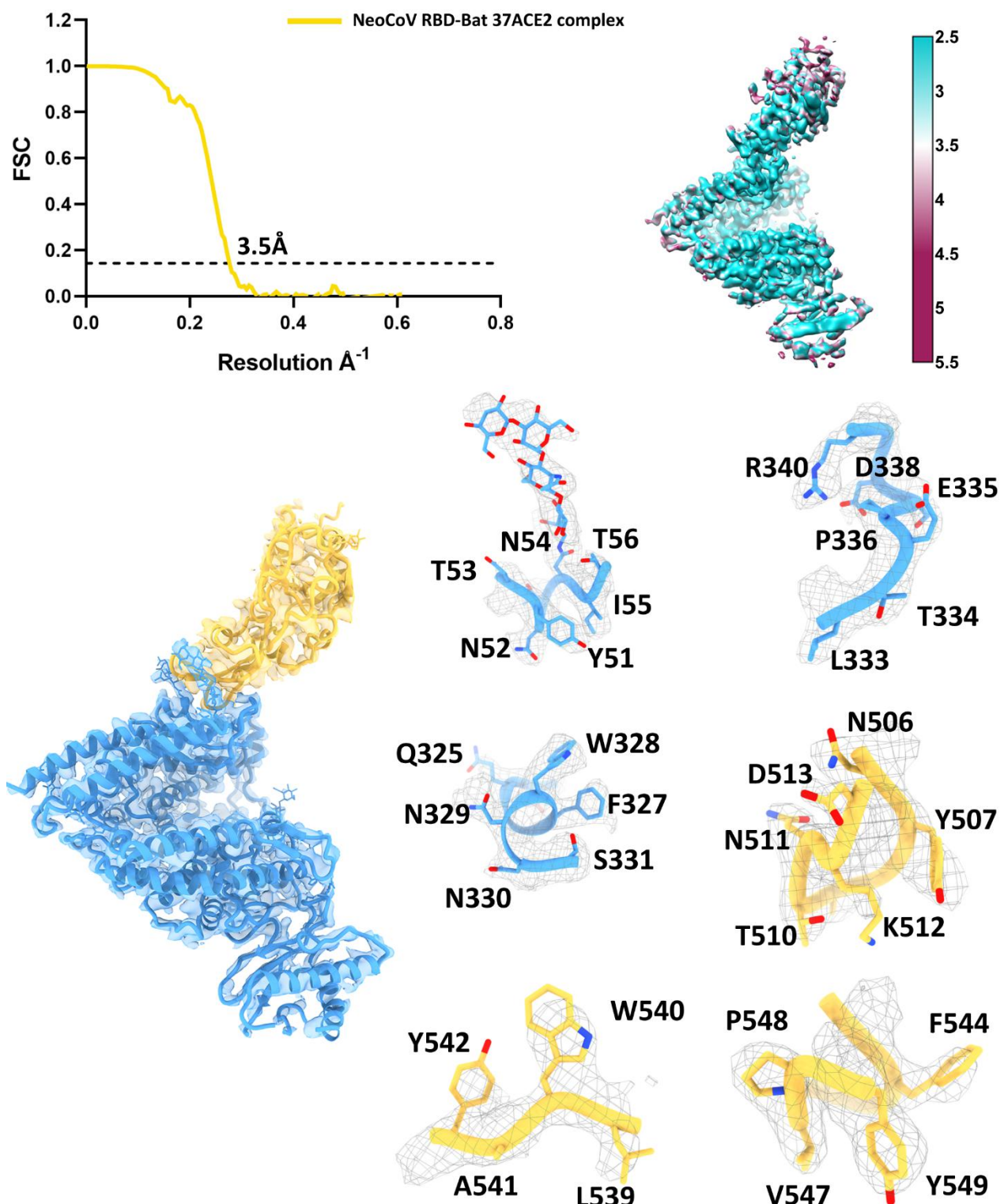


706

707 Extended data Figure 11 | Flowcharts for cryo-EM data processing of PDF-2180-CoV

708 RBD-Bat37ACE2 complex.

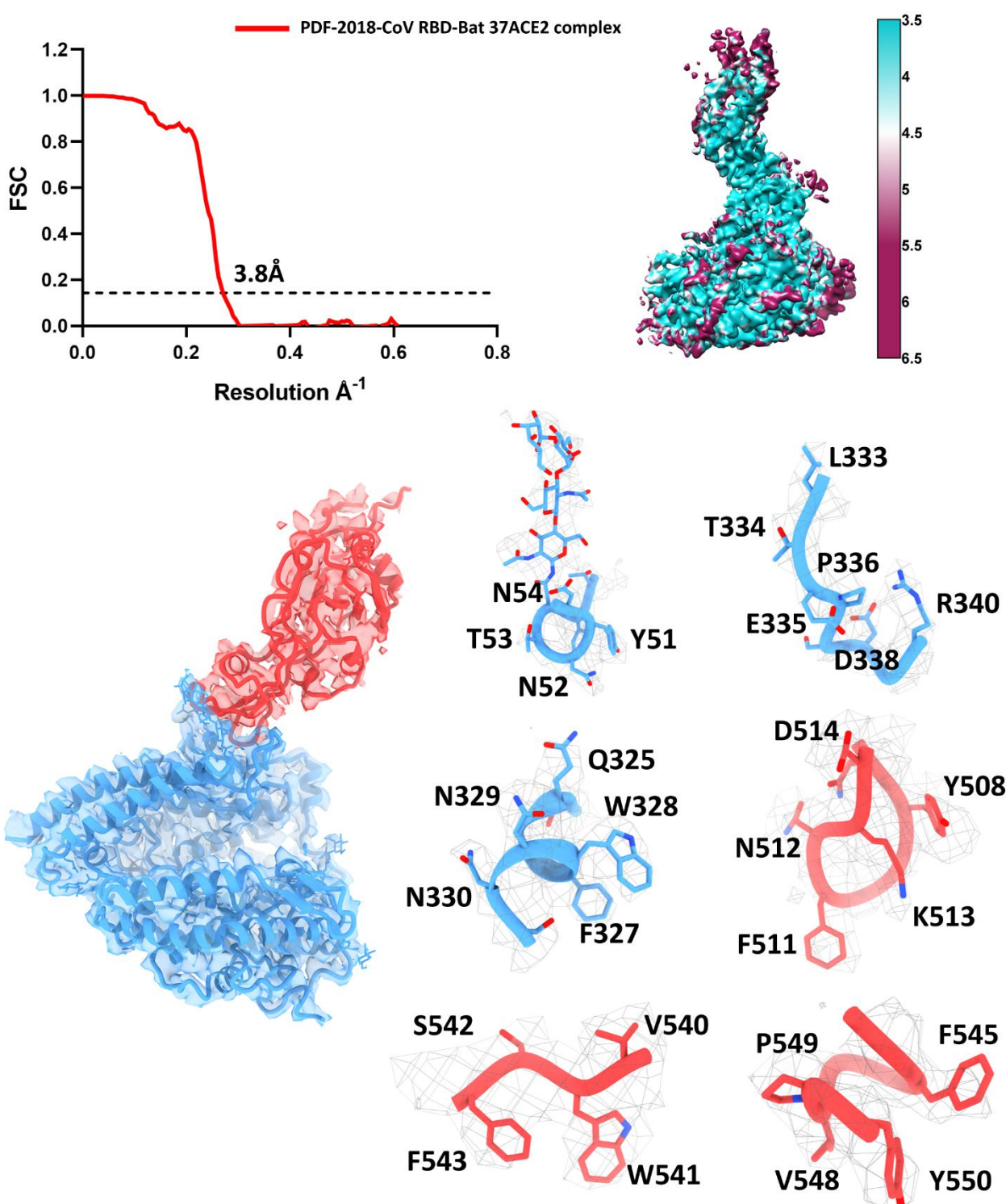
709



710

711 **Extended Data Figure 12 | Resolution Estimation of the EM maps, density maps, and atomics**
712 **models of NeoCoV RBD-Bat37ACE2 complex.**

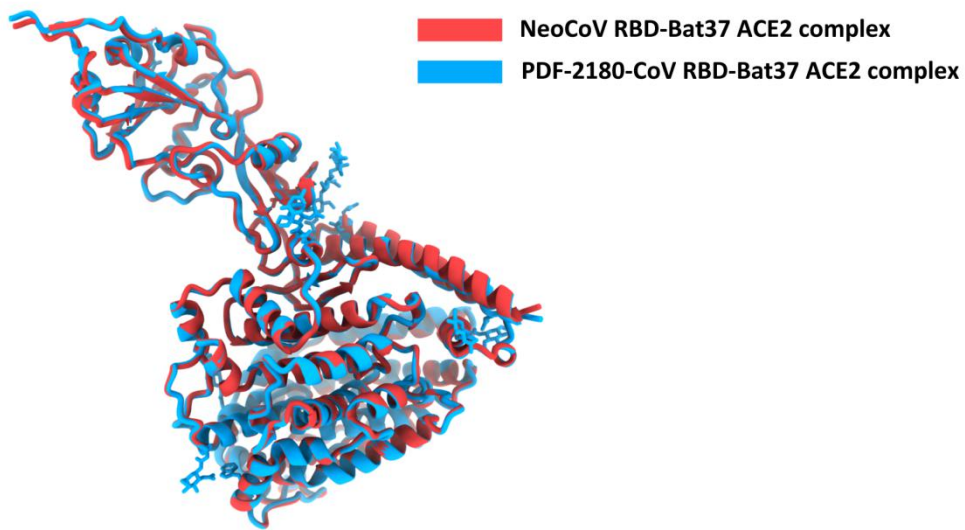
713



714

715 **Extended Data Figure 13 | Resolution Estimation of the EM maps, density maps, and atomics**
716 **models of PDF-2180-CoV RBD-Bat37ACE2 complex.**

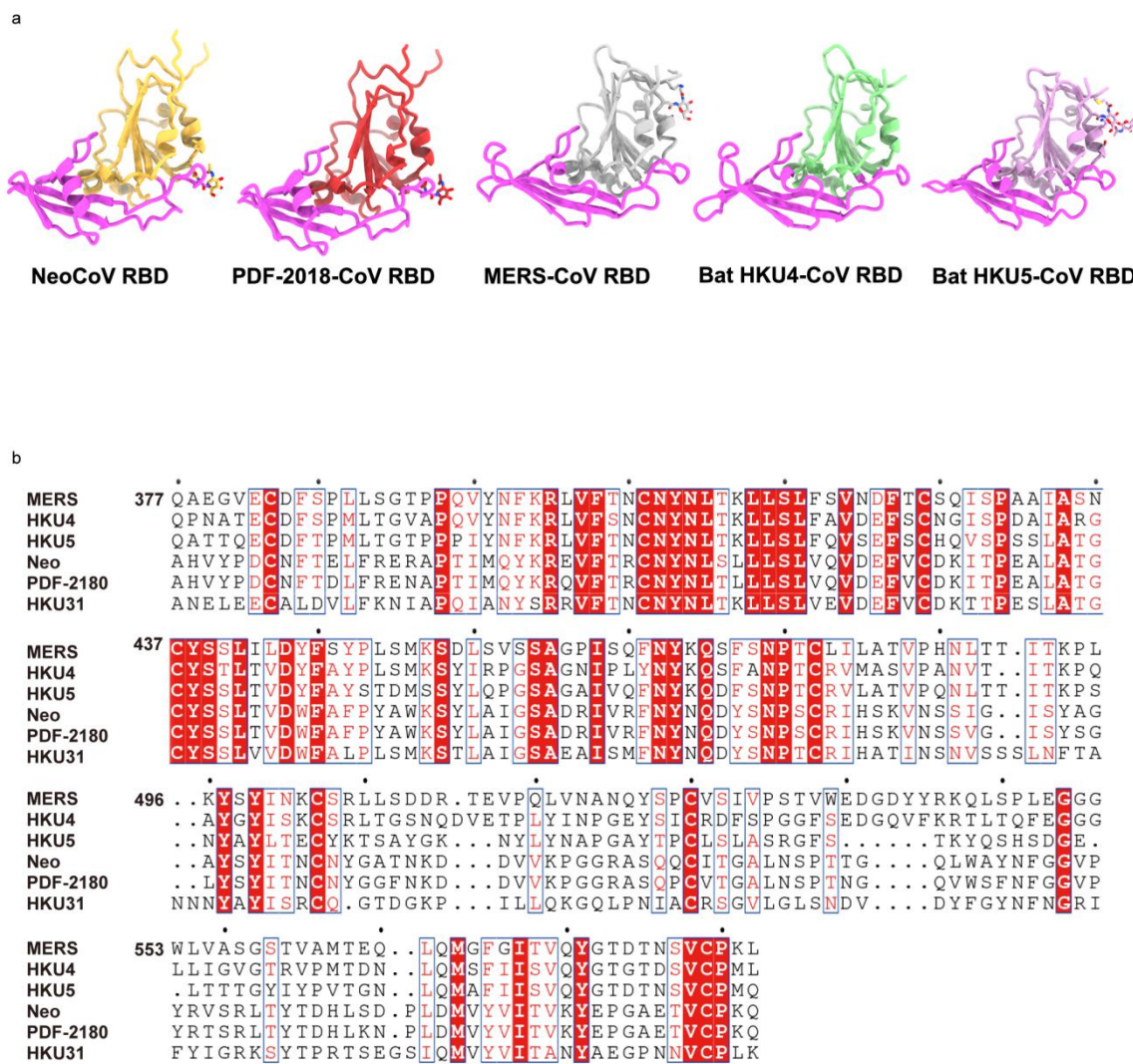
717



718

719 **Extended Data Figure 14 | Superimposition of overall structures of NeoCoV RBD-Bat37ACE2**
720 **complex (red) and PDF-2018-COV RBD-Bat37ACE2 complex (blue).**

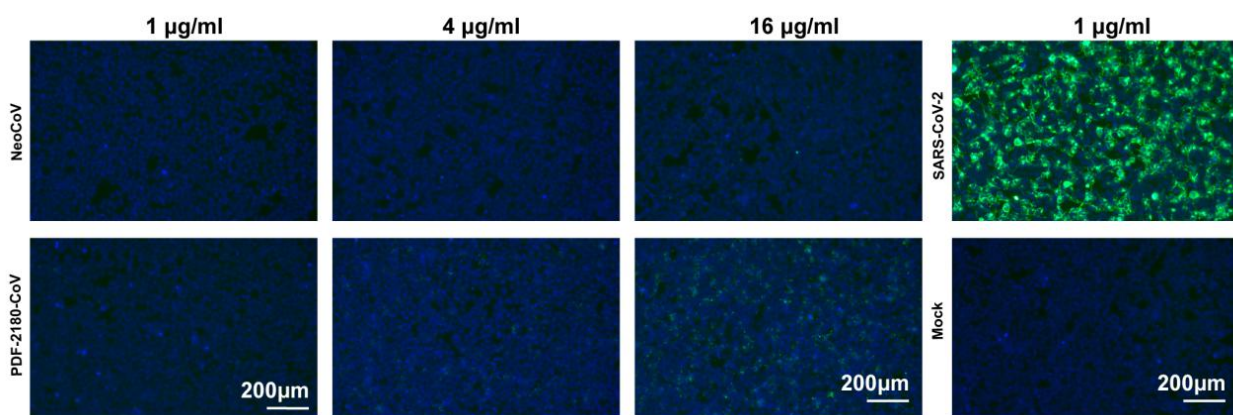
721



722

723 **Extended Data Figure 15 | Structures and sequence comparison of RBDs from different
724 merbecoviruses.**

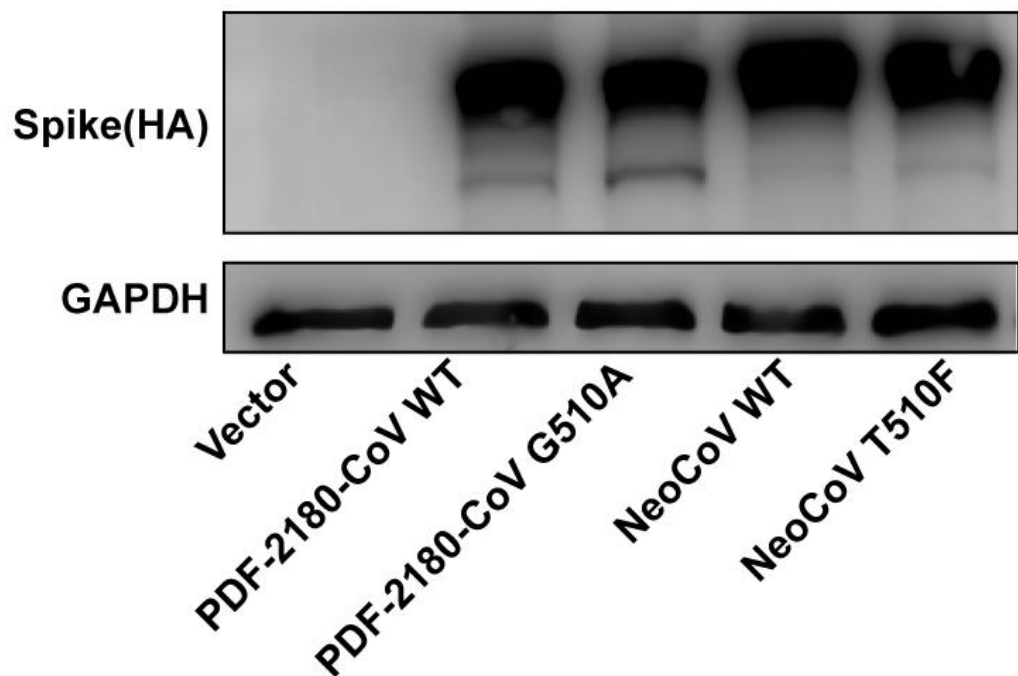
725



726

727 **Extended Data Figure 16 | Comparison of the binding affinity of NeoCoV and PDF-2180-CoV**
728 **RBD with hACE2 using SARS-CoV-2 RBD as a positive control.**

729

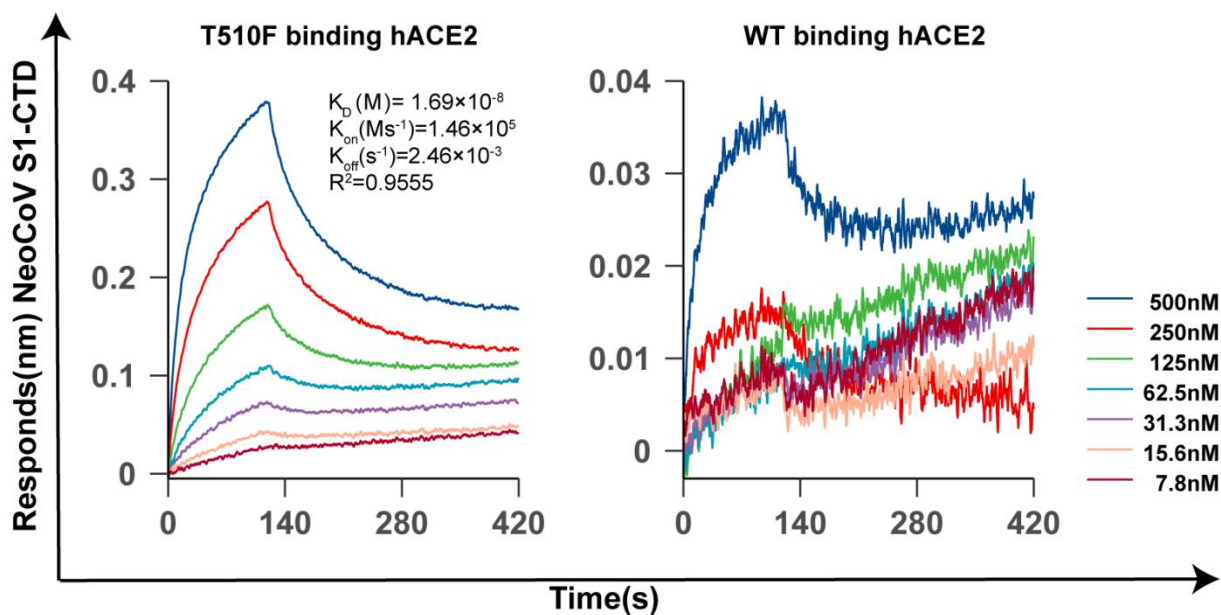


730

731 **Extended Data Figure 17 | Expression level of the NeoCoV and PDF-2180-CoV spike proteins**

732 **and their mutants.**

733



734

735 **Extended Data Figure 18 | BLI analysis of the binding kinetics of NeoCoV S1-CTD WT and**
736 **T510F interacting with human ACE2.**

737

738 **Extended Data table 1. Cryo-EM data collection and atomic model refinement statistics of RBD**
739 **mutant-mACE2 complex**
740

Data collection and reconstruction statistics

Protein	NeoCoV complex	RBD-Bat37ACE2	PDF-2018-CoV RBD-Bat37ACE2 complex
Voltage (kV)	300	300	
Detector	K2	K2	
Pixel size (Å)	1.04	1.04	
Electron dose (e ⁻ /Å ²)	60	60	
Defocus range (μm)	1.25-2.7	1.25-2.7	
Final particles	62, 545	130,308	
Resolution (Å)	3.5	3.8	

Models refinement and validation statistics

Ramachandran statistics		
Favored (%)	96.38	92.12
Allowed (%)	3.54	7.79
Outliers (%)	0.00	0.09
Rotamer outliers (%)	0.09	0.09
R.m.s.d		
Bond lengths (Å)	0.02	0.02
Bond angles (°)	1.26	1.26

741

742

743

Extended Data table 2. Residues of NeoCoV RBD interacting with Bat37ACE2 at the binding interface ($d < 4.5 \text{ \AA}$)

Bat37ACE2	NeoCoV RBD
Residues	Residues
E305	T510 K512
W328	A509
N329	G508 A509 G546 P548
S331	A509
M332	A509
L333	A509 T510
T334	A509 T510 N511
E335	N511
P336	N511
D338	N504 N506 L539
R340	N511 R550

747

748

749 **Extended Data table 3. Residues of PDF-2180-CoV RBD interacting with Bat37ACE2 at the**
750 **binding interface ($d < 4.5 \text{ \AA}$)**
751

Bat37ACE2	PDF-2180-CoV RBD
Residues	Residues
A304	F511
E305	F511 K513
F308	F511
W328	G510 F511
N329	G509 G510 G547 P549
N330	N544 G547 P549
S331	G510
M332	G510
L333	G510 F511
T334	F511 N512
E335	N512
P336	N512
D338	N505 N507 L540
R340	N512 R551

752

753 **Extended Data table 4. MD prediction of the effect of critical residue variations to the**
754 **interaction between NeoCoV and Bat37ACE2 by mCSM-PPI2.**
755

Substitution	$\Delta \Delta G$ (kcal/mol)									
	N504	G508	A509	T510	N511	K512	L539	G546	P548	R550
A	-0.087	-0.573		0.041	-0.477	-0.396	-0.22	-0.106	-0.646	-0.434
R	0.133	-0.849	0.261	0.196	-0.315	0.001	-0.273	-0.164	-0.152	
N		-0.515	0.466	0.078		0.015	-0.283	-0.008	-0.33	-0.369
D	0.098	-0.401	0.518	0.179	-0.038	-0.362	-0.257	0.219	-0.167	-0.543
C	-0.103	-0.805	0.148	-0.052	-0.525	-0.473	-0.261	-0.223	-0.385	-0.405
Q	0.113	-0.572	0.341	0.077	-0.577	0.211	-0.215	-0.007	-0.121	-0.285
E	0.294	-0.324	0.37	0.131	-0.277	-0.348	-0.302	0.21	0.006	-0.486
G	-0.129		-0.671	-0.102	-0.435	-0.543	-0.236		0.147	-0.591
H	0.156	-0.64	0.402	0.146	-0.065	-0.157	-0.064	-0.16	-0.304	-0.12
I	-0.182	-0.787	0.403	0.081	-0.184	-0.319	-0.178	-0.177	-0.403	-0.265
L	-0.137	-0.857	0.334	0.061	-0.123	-0.02		-0.189	-0.508	-0.269
K	0.27	-0.767	0.009	0.416	-0.722		-0.175	-0.098	-0.187	-0.113
M	-0.255	-0.682	-0.1	-0.001	-0.246	-0.325	-0.251	-0.105	-0.526	-0.311
F	-0.073	-0.476	1.012	0.487	-0.12	-0.134	0.287	-0.023	0.1504	-0.281
P	0.051	-0.712	-0.44	-0.149	-0.478	-0.41	-0.379	-0.125		-0.161
S	-0.101	-0.441	0.237	-0.011	-0.454	-0.17	-0.142	-0.082	-0.279	-0.3
T	-0.061	-0.567	0.342		-0.476	-0.226	-0.186	-0.077	-0.414	-0.32
W	-0.002	-0.158	1.396	0.481	0.033	-0.132	0.234	0.09	0.335	-0.066
Y	-0.072	-0.439	1.355	0.284	-0.083	-0.065	0.204	0.02	0.1918	-0.282
V	-0.086	-0.673	0.025	0.003	-0.341	-0.408	0.031	-0.082	-0.563	-0.405

756

- 757 1 Raj, V. S. *et al.* Dipeptidyl peptidase 4 is a functional receptor for the emerging human
758 coronaviruses-EMC. *Nature* **495**, 251-254, doi:10.1038/nature12005 (2013).
- 759 2 Yang, Y. *et al.* Receptor usage and cell entry of bat coronavirus HKU4 provide insight into
760 bat-to-human transmission of MERS coronavirus. *Proc Natl Acad Sci U S A* **111**, 12516-12521,
761 doi:10.1073/pnas.1405889111 (2014).
- 762 3 Lau, S. K. P. *et al.* Receptor Usage of a Novel Bat Lineage C Betacoronavirus Reveals Evolution
763 of Middle East Respiratory Syndrome-Related Coronavirus Spike Proteins for Human
764 Dipeptidyl Peptidase 4 Binding. *J Infect Dis* **218**, 197-207, doi:10.1093/infdis/jiy018 (2018).
- 765 4 Luo, C. M. *et al.* Discovery of Novel Bat Coronaviruses in South China That Use the Same
766 Receptor as Middle East Respiratory Syndrome Coronavirus. *J Virol* **92**,
767 doi:10.1128/JVI.00116-18 (2018).
- 768 5 Ithete, N. L. *et al.* Close relative of human Middle East respiratory syndrome coronavirus in
769 bat, South Africa. *Emerg Infect Dis* **19**, 1697-1699, doi:10.3201/eid1910.130946 (2013).
- 770 6 Cui, J., Li, F. & Shi, Z. L. Origin and evolution of pathogenic coronaviruses. *Nat Rev Microbiol*
771 **17**, 181-192, doi:10.1038/s41579-018-0118-9 (2019).
- 772 7 Li, W. *et al.* Broad receptor engagement of an emerging global coronavirus may potentiate
773 its diverse cross-species transmissibility. *Proc Natl Acad Sci U S A* **115**, E5135-E5143,
774 doi:10.1073/pnas.1802879115 (2018).
- 775 8 Lednicky, J. A. *et al.* Independent infections of porcine deltacoronavirus among Haitian
776 children. *Nature* **600**, 133-137, doi:10.1038/s41586-021-04111-z (2021).
- 777 9 Latinne, A. *et al.* Origin and cross-species transmission of bat coronaviruses in China. *Nat
778 Commun* **11**, 4235, doi:10.1038/s41467-020-17687-3 (2020).
- 779 10 Wong, A. C. P., Li, X., Lau, S. K. P. & Woo, P. C. Y. Global Epidemiology of Bat Coronaviruses.
780 *Viruses* **11**, doi:10.3390/v11020174 (2019).
- 781 11 Ksiazek, T. G. *et al.* A novel coronavirus associated with severe acute respiratory syndrome. *N
782 Engl J Med* **348**, 1953-1966, doi:10.1056/NEJMoa030781 (2003).
- 783 12 Zaki, A. M., van Boheemen, S., Bestebroer, T. M., Osterhaus, A. D. & Fouchier, R. A. Isolation
784 of a novel coronavirus from a man with pneumonia in Saudi Arabia. *N Engl J Med* **367**,
785 1814-1820, doi:10.1056/NEJMoa1211721 (2012).
- 786 13 Zhou, P. *et al.* A pneumonia outbreak associated with a new coronavirus of probable bat
787 origin. *Nature* **579**, 270-273, doi:10.1038/s41586-020-2012-7 (2020).
- 788 14 Chen, L. *et al.* RNA based mNGS approach identifies a novel human coronavirus from two
789 individual pneumonia cases in 2019 Wuhan outbreak. *Emerg Microbes Infect* **9**, 313-319,
790 doi:10.1080/22221751.2020.1725399 (2020).
- 791 15 WHO. Middle East respiratory syndrome coronavirus (MERS-CoV),
792 <<http://www.who.int/emergencies/mers-cov/en/>> (
- 793 16 Mohd, H. A., Al-Tawfiq, J. A. & Memish, Z. A. Middle East Respiratory Syndrome Coronavirus
794 (MERS-CoV) origin and animal reservoir. *Virol J* **13**, 87, doi:10.1186/s12985-016-0544-0
795 (2016).
- 796 17 Li, F. Receptor recognition mechanisms of coronaviruses: a decade of structural studies. *J
797 Virol* **89**, 1954-1964, doi:10.1128/JVI.02615-14 (2015).
- 798 18 Li, W. *et al.* Angiotensin-converting enzyme 2 is a functional receptor for the SARS
799 coronavirus. *Nature* **426**, 450-454, doi:10.1038/nature02145 (2003).
- 800 19 Yeager, C. L. *et al.* Human aminopeptidase N is a receptor for human coronavirus 229E.

- 801 20 *Nature* **357**, 420-422, doi:10.1038/357420a0 (1992).
- 802 20 Williams, R. K., Jiang, G. S. & Holmes, K. V. Receptor for mouse hepatitis virus is a member of
803 the carcinoembryonic antigen family of glycoproteins. *Proc Natl Acad Sci U S A* **88**,
804 5533-5536, doi:10.1073/pnas.88.13.5533 (1991).
- 805 21 Tsai, J. C., Zelus, B. D., Holmes, K. V. & Weiss, S. R. The N-terminal domain of the murine
806 coronavirus spike glycoprotein determines the CEACAM1 receptor specificity of the virus
807 strain. *J Virol* **77**, 841-850, doi:10.1128/jvi.77.2.841-850.2003 (2003).
- 808 22 Hofmann, H. et al. Human coronavirus NL63 employs the severe acute respiratory syndrome
809 coronavirus receptor for cellular entry. *Proc Natl Acad Sci U S A* **102**, 7988-7993,
810 doi:10.1073/pnas.0409465102 (2005).
- 811 23 Anthony, S. J. et al. Further Evidence for Bats as the Evolutionary Source of Middle East
812 Respiratory Syndrome Coronavirus. *mBio* **8**, doi:10.1128/mBio.00373-17 (2017).
- 813 24 Corman, V. M. et al. Characterization of a novel betacoronavirus related to middle East
814 respiratory syndrome coronavirus in European hedgehogs. *J Virol* **88**, 717-724,
815 doi:10.1128/JVI.01600-13 (2014).
- 816 25 Lau, S. K. P. et al. Identification of a Novel Betacoronavirus (Merbecovirus) in Amur
817 Hedgehogs from China. *Viruses* **11**, doi:10.3390/v11110980 (2019).
- 818 26 Corman, V. M. et al. Rooting the phylogenetic tree of middle East respiratory syndrome
819 coronavirus by characterization of a conspecific virus from an African bat. *J Virol* **88**,
820 11297-11303, doi:10.1128/JVI.01498-14 (2014).
- 821 27 Geldenhuys, M. et al. A metagenomic viral discovery approach identifies potential zoonotic
822 and novel mammalian viruses in Neoromicia bats within South Africa. *PLoS One* **13**,
823 e0194527, doi:10.1371/journal.pone.0194527 (2018).
- 824 28 Menachery, V. D. et al. Trypsin Treatment Unlocks Barrier for Zoonotic Bat Coronavirus
825 Infection. *J Virol* **94**, doi:10.1128/JVI.01774-19 (2020).
- 826 29 Adams, D. J., Spendlove, J. C., Spendlove, R. S. & Barnett, B. B. Aerosol stability of infectious
827 and potentially infectious reovirus particles. *Appl Environ Microbiol* **44**, 903-908,
828 doi:10.1128/aem.44.4.903-908.1982 (1982).
- 829 30 Whitt, M. A. Generation of VSV pseudotypes using recombinant DeltaG-VSV for studies on
830 virus entry, identification of entry inhibitors, and immune responses to vaccines. *J Virol Methods* **169**, 365-374, doi:10.1016/j.jviromet.2010.08.006 (2010).
- 832 31 Yan, H. et al. ACE2 receptor usage reveals variation in susceptibility to SARS-CoV and
833 SARS-CoV-2 infection among bat species. *Nat Ecol Evol* **5**, 600-608,
834 doi:10.1038/s41559-021-01407-1 (2021).
- 835 32 Ishikawa, H., Meng, F., Kondo, N., Iwamoto, A. & Matsuda, Z. Generation of a dual-functional
836 split-reporter protein for monitoring membrane fusion using self-associating split GFP.
837 *Protein Eng Des Sel* **25**, 813-820, doi:10.1093/protein/gzs051 (2012).
- 838 33 Rodrigues, C. H. M., Myung, Y., Pires, D. E. V. & Ascher, D. B. mCSM-PPI2: predicting the
839 effects of mutations on protein-protein interactions. *Nucleic Acids Res* **47**, W338-W344,
840 doi:10.1093/nar/gkz383 (2019).
- 841 34 Du, Y. et al. A broadly neutralizing humanized ACE2-targeting antibody against SARS-CoV-2
842 variants. *Nat Commun* **12**, 5000, doi:10.1038/s41467-021-25331-x (2021).
- 843 35 Wrapp, D. et al. Structural Basis for Potent Neutralization of Betacoronaviruses by
844 Single-Domain Camelid Antibodies. *Cell* **181**, 1004-1015 e1015,

- 845 doi:10.1016/j.cell.2020.04.031 (2020).

846 36 Liu, Y., Gayle, A. A., Wilder-Smith, A. & Rocklov, J. The reproductive number of COVID-19 is
847 higher compared to SARS coronavirus. *J Travel Med* **27**, doi:10.1093/jtm/taaa021 (2020).

848 37 Liu, Y. & Rocklov, J. The reproductive number of the Delta variant of SARS-CoV-2 is far higher
849 compared to the ancestral SARS-CoV-2 virus. *J Travel Med* **28**, doi:10.1093/jtm/taab124
850 (2021).

851 38 Nishiura, H. *et al.* Relative Reproduction Number of SARS-CoV-2 Omicron (B.1.1.529)
852 Compared with Delta Variant in South Africa. *J Clin Med* **11**, doi:10.3390/jcm11010030
853 (2021).

854 39 Baric, R. S., Fu, K., Schaad, M. C. & Stohlman, S. A. Establishing a genetic recombination map
855 for murine coronavirus strain A59 complementation groups. *Virology* **177**, 646-656,
856 doi:10.1016/0042-6822(90)90530-5 (1990).

857 40 Banner, L. R., Keck, J. G. & Lai, M. M. A clustering of RNA recombination sites adjacent to a
858 hypervariable region of the peplomer gene of murine coronavirus. *Virology* **175**, 548-555,
859 doi:10.1016/0042-6822(90)90439-x (1990).

860 41 Chu, D. K. *et al.* MERS coronaviruses in dromedary camels, Egypt. *Emerg Infect Dis* **20**,
861 1049-1053, doi:10.3201/eid2006.140299 (2014).

862 42 Harvey, W. T. *et al.* SARS-CoV-2 variants, spike mutations and immune escape. *Nat Rev
863 Microbiol* **19**, 409-424, doi:10.1038/s41579-021-00573-0 (2021).

864 43 Callaway, E. Heavily mutated Omicron variant puts scientists on alert. *Nature* **600**, 21,
865 doi:10.1038/d41586-021-03552-w (2021).

866 44 Schwegmann-Wessels, C. *et al.* Comparison of vesicular stomatitis virus pseudotyped with
867 the S proteins from a porcine and a human coronavirus. *J Gen Virol* **90**, 1724-1729,
868 doi:10.1099/vir.0.009704-0 (2009).

869 45 Wang, J., Kondo, N., Long, Y., Iwamoto, A. & Matsuda, Z. Monitoring of HIV-1
870 envelope-mediated membrane fusion using modified split green fluorescent proteins. *J Virol
871 Methods* **161**, 216-222, doi:10.1016/j.jviromet.2009.06.017 (2009).

872 46 Scheres, S. H. RELION: implementation of a Bayesian approach to cryo-EM structure
873 determination. *J Struct Biol* **180**, 519-530, doi:10.1016/j.jsb.2012.09.006 (2012).

874 47 Brown, A. *et al.* Tools for macromolecular model building and refinement into electron
875 cryo-microscopy reconstructions. *Acta Crystallogr D Biol Crystallogr* **71**, 136-153,
876 doi:10.1107/S1399004714021683 (2015).

877 48 Afonine, P. V. *et al.* Towards automated crystallographic structure refinement with
878 phenix.refine. *Acta Crystallogr D Biol Crystallogr* **68**, 352-367,
879 doi:10.1107/S0907444912001308 (2012).

880 49 L.J. REED, H. M. A SIMPLE METHOD OF ESTIMATING FIFTY PER CENT ENDPOINTS. *American
881 Journal of Epidemiology* **27**, 493-497 (1938).

882 50 Nie, J. *et al.* Quantification of SARS-CoV-2 neutralizing antibody by a pseudotyped
883 virus-based assay. *Nat Protoc* **15**, 3699-3715, doi:10.1038/s41596-020-0394-5 (2020).